

525677  
27/

## **Carbon dioxide clouds at high altitude in the tropics and in an early dense Martian atmosphere**

Anthony Colaprete<sup>1</sup>  
Owen B. Toon<sup>2, 3</sup>

<sup>1</sup> NASA Ames Research Center  
Moffett Field, SST MS 245-3, Mountain View, CA  
(650) 604-2918  
[tonyc@hellas.arc.nasa.gov](mailto:tonyc@hellas.arc.nasa.gov)

<sup>2</sup> Laboratory for Atmospheric and Space Physics

<sup>3</sup> Program in Atmospheric and Oceanic Sciences  
University of Colorado, Boulder, CO 80309

February, 2001

## Abstract

We use a time dependent, microphysical cloud model to study the formation of carbon dioxide clouds in the Martian atmosphere. Laboratory studies by Glandorf et al. (this issue) show that high critical supersaturations are required for cloud particle nucleation and that surface kinetic growth is not limited. These conditions, which are similar to those for cirrus clouds on Earth, lead to the formation of carbon dioxide ice particles with radii greater than 500  $\mu\text{m}$  and concentrations less than 0.1  $\text{cm}^{-3}$  for typical atmospheric conditions. Within the current Martian atmosphere,  $\text{CO}_2$  cloud formation is possible at the poles during winter and at high altitudes in the tropics during periods of increased atmospheric dust loading. In both cases, temperature perturbations of several degrees below the  $\text{CO}_2$  saturation temperature are required to nucleate new cloud particles suggesting that dynamical processes are the most common initiators of carbon dioxide clouds rather than diabatic cooling. The microphysical cloud model, coupled to a two-stream radiative transfer model, is used to reexamine the impact of  $\text{CO}_2$  clouds on the surface temperature within a dense  $\text{CO}_2$  atmosphere. The formation of carbon dioxide clouds leads to a warmer surface than what would be expected for clear sky conditions. The amount of warming is sensitive to the presence of dust and water vapor in the atmosphere, both of which act to dampen cloud effects. The radiative warming associated with cloud formation, as well as latent heating, work to dissipate the clouds when present. Thus, clouds never last for periods much longer than several days, limiting their overall effectiveness for warming the surface. The time average cloud optical depth is approximately unity leading to a 5 - 10 K warming, depending on the surface pressure. However, the surface temperature does not rise above the freezing point of liquid water even for pressures as high as 5 bars, at a solar luminosity of 75% the current value.

## 1. Introduction

The presence and properties of carbon dioxide clouds within the Martian atmosphere have been the subject of debate since the Mariner 6 and 7 infrared spectrometer (IRS) equatorial limb observations of a scattered sunlight spike at 4.26  $\mu\text{m}$  were attributed to solid  $\text{CO}_2$  at altitudes between 18 and 32 km (Herr and Pimentel, 1970). The Viking Infrared Thermal Mapper (IRTM) measured equatorial temperatures 50 K too warm for  $\text{CO}_2$  condensation to occur at these altitudes, calling the Mariner findings into question. Other indirect evidence for carbon dioxide clouds includes the Mariner 9 Infrared Interferometer Spectrometer (IRIS) temperature profiles of the north polar hood (Briggs and Leovy, 1978) and the extremely low Viking IRTM brightness temperatures observed in polar regions (Kieffer et al. 1976). The low temperatures measured in both of these instances are consistent with  $\text{CO}_2$  cloud formation. The IRIS temperature profile indicated areas of the polar atmosphere at or near the condensation point of carbon dioxide, while the IRTM measurements of extremely low brightness temperatures (128 K to 134 K) may be the result of scattering  $\text{CO}_2$  cloud particles. More recently, telescopic measurements in the near infrared (Bell et al. 1996), have detected absorption features resulting from the presence of solid "fine" grained  $\text{CO}_2$ , some of which may be in the form of cloud particles. Clancy and Sandor (1998) have also suggested that the blue colored clouds observed by the Imager for Mars Pathfinder (IMP) were composed of carbon dioxide. The color of the clouds, they argued, is the result of scattering from small (0.1 - 0.3  $\mu\text{m}$ )  $\text{CO}_2$  ice particles with particle concentrations on order of 100  $\text{cm}^{-3}$ , forming at altitudes between 60 - 80 km. However, Colaprete et al. (1998) argued that water ice clouds reflecting Rayleigh scattered light from the air are more likely responsible for the blue coloration.

While it is generally accepted that carbon dioxide clouds form in the Martian atmosphere, their microphysical properties, as well as how, when and where they form are still not understood. The formation process, including the nucleation of new particles and the growth of existing particles via condensation, will greatly effect the deposition of CO<sub>2</sub> onto the polar caps and the polar energy budget within the current Martian atmosphere. Furthermore, infrared scattering by carbon dioxide clouds has been suggested as a possible factor in resolving the "early warmer, wetter Mars" paradox (Forget and Pierrehumbert, 1997). Clouds consisting of large ( $> 10 \mu\text{m}$ ) carbon dioxide ice crystals may have substantial infrared scattering greenhouse effects, which, under early Martian atmospheric conditions, could warm the planet's surface to above freezing. Whether these clouds provide a warming or a cooling effect depends strongly on the size and geographic distribution of the ice particles, as well as the total cloud optical depth. In turn these characteristics depend on details of cloud microphysics and the atmospheric processes that leads to cloud formation.

In this paper we first review the nucleation physics of carbon dioxide cloud particles given recently measured constraints on the critical saturation level and contact parameter (Glandorf et al., this issue). Using a one-dimensional, time dependent microphysical cloud model, we explore the size and number concentration of cloud crystals that may form under different atmospheric conditions. Secondly, using this microphysical cloud model coupled to a 1-D radiative-convective model, we address several existing questions regarding the role of carbon dioxide clouds in dense CO<sub>2</sub> atmospheres. The first set of questions deals with the formation of the clouds themselves. At what altitude will carbon dioxide clouds form? How long do they persist? What fraction of the planet will be cloudy? The second set of questions concern themselves with the climate effects of these clouds. Kasting (1991) proposed that any increase in carbon dioxide above a surface pressure of about 0.35 bars (at current solar luminosities) would lead to saturation, cloud formation and a surface cooling. The addition of more CO<sub>2</sub> ultimately leads to cloud formation and surface cooling so that a "run away" condensation takes place, limiting the amount of green house warming that may be achieved by adding more and more CO<sub>2</sub>. What is the radiative effect of the clouds on the atmosphere and surface? Does condensation limit the amount of greenhouse warming afforded by a thick CO<sub>2</sub> atmosphere? Ultimately we will address the underling question of whether or not carbon dioxide clouds significantly warm or cool a planet.

## 2.0 Nucleation Theory

Little is known about the physics of carbon dioxide particle formation. Until recently the physical parameters of classic nucleation theory, such as the contact angle and the critical supersaturation, were only estimated from theory. Below we briefly discuss the process of nucleation as it pertains to CO<sub>2</sub> cloud formation on Mars.

The process of nucleation describes the initial formation of a crystal spontaneously (homogeneous nucleation) or on a dust grain or similar aerosol (heterogeneous nucleation). The homogenous nucleation of most vapors requires very high levels of

saturation, as the energy barrier involved with forming clusters of molecules is high. If a pre-existing surface is involved, as is the case with heterogeneous nucleation, the surface energy per molecule is greatly reduced and the vapor saturation level needed to nucleate decreases by as much as two orders of magnitude from that of homogeneous nucleation. For this reason, in the simulations developed here we only consider the nucleation of CO<sub>2</sub> onto dust grains coated with a thin layer of preexisting water ice (Glandorf et al., this issue).

These nucleation processes are not unique to Mars. For instance, there is much current research on water ice formation in the Earth's atmosphere. It has been found that the Earth's upper troposphere is often highly supersaturated, which is why contrails occur (Jensen et al., 1998). Observations and theories both show that liquid sulfate aerosols can freeze to produce ice crystals at supersaturations more than 50% (Jensen et al. 1998; Tabazadeh et al., 1997). Such liquid aerosols will not be present on Mars. However, ice nuclei on Earth, composed in part of mineral grains also serve to promote ice formation (Jensen et al., 1998). As we shall discuss below relatively high supersaturations must also occur on Mars for CO<sub>2</sub> ice to form.

## 2.1 Heterogeneous Nucleation

Heterogeneous nucleation is highly selective for particle size and depends greatly on the contact parameter  $m$  and the supersaturation  $S = s-1$ , where the saturation,  $s$ , is the ratio of the partial pressure of CO<sub>2</sub> vapor to the vapor pressure of CO<sub>2</sub> ice. The rate of nucleation (Pruppacher and Klett, 1978) may be written as

$$J = \frac{4\pi^2 r_{cn}^2 Z_s e}{(2\pi \ln kT)^{3/2}} a_g^2 c_l \exp \left[ \frac{(\Delta F_{des} - \Delta F_{sd} - f\Delta F_g)}{kT} \right] \quad 2.1$$

where  $r_{cn}$  is the radius of the dry nucleus,  $e$  is the partial pressure of CO<sub>2</sub> vapor,  $a_g$  is the critical germ radius,  $c_l$  is the concentration of adsorbing CO<sub>2</sub> molecules,  $T$  is the temperature, and  $k$  is Boltzman's constant.  $Z_s$ , the Zeldovitch factor, is a correction to the equilibrium equation for nucleation. This expression is dominated by the exponential term that contains the free energies of activation for desorption ( $\Delta F_{des}$ ), for surface diffusion ( $\Delta F_{sd}$ ) and for germ formation ( $\Delta F_g$ ) with homogeneous nucleation. Contact between the nucleating molecule and the substrate surface changes the free energy of germ formation and is accounted for by the factor  $f$ . This variable relates the surface geometry of the substrate to the surface free energies of vapor and ice. For a curved surface  $f$  is given by:

$$2f = 1 + \left( \frac{1-Xm}{g} \right)^3 + X^3 \left[ 2 - 3 \left( \frac{X-m}{g} \right) + \left( \frac{X-m}{g} \right)^3 \right] + 3X^2 m \left( \frac{X-m}{g} - 1 \right) \quad 2.2$$

where  $g = (1+X^2-2Xm)^{1/2}$  and  $X = r_{cn}/a_g$ . The amount  $f$  changes the free energy of germ formation depends on the value of the contact parameter,  $m$ , described below.

## 2.2 Contact Parameter

The variance in interfacial energies between the molecule and the substrate, the difference between nucleation on a flat surface and on a highly curved surface such as a small dust grain for instance, can greatly effect the energy of germ formation. This variance can be parameterized as the cosine of a "contact angle" and calculated from the ratio of free energies,  $\sigma$ :

$$m = \frac{\sigma_{cn/v} - \sigma_{cn/i}}{\sigma_{i/v}} \quad 2.3$$

where the subscripts *cn*, *v*, and *i* designate the substrate, vapor, and ice respectively. The contact parameter can be thought of in a physical sense as the amount of contact between the dust grain and the water cluster. The contact parameter is determined by a mechanical equilibrium such that there is no net force component along the surface of the solid. For a contact parameter of  $m = 1$ , every vapor molecule which comes into contact with the dust grain will be nucleated. The value of  $m$  varies widely with the type of material nucleating. For example, the contact parameter for water ice and silver iodide, a popular cloud seeding agent, is  $m = 0.956 - 0.988$ . For liquid water nucleating onto a typical soil  $m = 0.36 - 0.42$  (Pruppacher and Klett, 1978). The roughness and microscopic makeup of the nucleating surface can dramatically change the value of  $m$ . Terrestrial clays, a possible analog to the Martian dust, are very susceptible to absorbing impurities that can increase their nucleation efficiency. For instance, when ice has formed once on a dust grain the contact parameter can increase substantially (Roberts and Hallett, 1968). Until recently, only estimates of the contact parameter for CO<sub>2</sub> ice had been made. Wood (1998) estimated a contact parameter of  $m > 0.87$  by comparing calculations of the disregistry between CO<sub>2</sub> ice and candidate Martian dust minerals (Gooding, 1986) with the disregistry for water ice (Pruppacher and Klett, 1978).

### 2.3 Supersaturation

The critical germ radius and the free energy associated with forming this germ are strongly dependent on the level of CO<sub>2</sub> supersaturation. The critical germ radius,  $a_g$ , and the free energy of germ formation,  $\Delta F_g$ , are given by

$$a_g = \frac{2M\sigma}{RT\rho \ln(S+1)} \quad 2.4$$

$$\Delta F_g = \frac{4\pi a_g^2 \sigma}{3} \quad 2.5$$

In these two expressions  $M$  is the molecular weight of CO<sub>2</sub>,  $\sigma$  is the surface free energy of CO<sub>2</sub> ice,  $R$  the gas constant,  $\rho$  the density of CO<sub>2</sub> ice, and  $S$  the supersaturation. The nucleation rate for CO<sub>2</sub> is shown in Figure 1 as a function of both contact parameter and supersaturation.

In general, for a given radius and contact angle, as the supersaturation increases, the free energy of germ formation decreases and nucleation rate (Eq. 2.1) increases quickly. When the nucleation rate is on order  $J = 1 \text{ sec}^{-1}$  the supersaturation is said to be at the "critical saturation" for nucleation. The nucleation rate is a strong function of the size of the particle on which nucleation is occurring (Fig. 1). Ultimately the supersaturation (which is normally driven by uplift velocity) determines the smallest particle that will become a cloud particle. For higher values of  $m$ , nucleation will occur at lower supersaturation. Once nucleation occurs, the  $\text{CO}_2$  vapor abundance is quickly reduced by condensation bringing the supersaturation down. As the supersaturation approaches zero the nucleation rate decreases rapidly, effectively stopping further nucleation. Because of its strong dependence on the supersaturation, nucleation ultimately limits the number of particles and the size of the particles that can form within a carbon dioxide cloud.

Glandorf et al. (this issue) examined these issues experimentally. The critical saturation ratio required for carbon dioxide to nucleate onto ice was measured to be approximately 1.35 at Martian temperatures. That is, the  $\text{CO}_2$  vapor needed to be supersaturated by 35 % before nucleation would occur. From this measurement, using the nucleation theory described above, an approximate contact parameter of  $m = 0.95$  between water ice and  $\text{CO}_2$  under Martian conditions was also determined. To understand the effects these measured nucleation parameters would have on Martian  $\text{CO}_2$  cloud formation several simulations were conducted (Fig. 2, 3). For these simulations dust was assumed to be distributed vertically with a scale height of 12.5 km and to have a log normal size distribution with a modal radius of  $r_o = 1.0 \text{ } \mu\text{m}$  and standard deviation of  $\sigma = 1.8$ . We assumed water ice coated dust particles, but did not specifically simulate the water ice condensation. The purpose of these first simulations is to understand the effects of the nucleation and growth properties measured by Glandorf et al. (this issue) on cloud particle formation. Therefore, no vertical transport of particles, either by sedimentation or diffusion, was performed. Rather, just the nucleation and condensation rates for distributions of particles under Martian temperatures and pressures were calculated. The release of latent heat was included but proved not to be important since no re-supply of  $\text{CO}_2$  vapor was permitted.

At the high saturation ratios needed for nucleation, once a particle is nucleated, condensation growth occurs very rapidly reducing  $S$  and leading to the all of the vapor being condensed onto a small number of large particles. Figure 2 shows the effective particle radius (the cross section weighted average particle size) for three contact parameters as a function of atmospheric cooling rate. These model simulations were conducted at an initial  $\text{CO}_2$  pressure of 6.4 mbar and an initial temperature of 150 K. For larger contact parameters smaller dust particles will nucleate more readily than for smaller contact parameters. Estimates of the contact parameter in this work placed the value near 0.95, however, a small difference in the contact parameter can lead to a large difference in the nucleation rate, and hence, the overall effective particle size. Also affecting the particle size is the rate at which the ambient air is cooled. As the air cools to the point that the critical saturation ratio for nucleation is achieved, the largest condensation nuclei (CN) preferentially nucleate first and quickly drop the saturation ratio below the critical saturation ratio, thereby stopping any further nucleation of smaller

particles. Therefore, for slow cooling rates, like those achieved by radiative cooling during the polar night ( $\sim 1$  K/day), very large particles at low concentrations are expected. Higher cooling rates, like those possibly achieved in mountain waves, can lead to smaller particles as the rate of saturation increase due to cooling becomes faster than the rate of saturation decrease due to condensation, allowing saturation ratios greater than the critical saturation ratio for longer periods of time. However, at surface pressures, cooling rates as high as  $\sim 100$  K/Day still produce cloud particles with sizes of about  $100\text{ }\mu\text{m}$  in less than 10 minutes.

It should be noted that the presence of large particles on Mars does not depend upon the details of the nucleation rate equation (Eq. 2.1). Rather it is a simple consequence of mass conservation. While several others have made analogies between cirrus clouds on Earth and  $\text{CO}_2$  clouds on Mars, in fact there is an important difference. While both  $\text{CO}_2$  and  $\text{H}_2\text{O}$  need supersaturations of tens of percent to form clouds, the mass of  $\text{CO}_2$  vapor on Mars is at least three orders of magnitude higher than the mass of water vapor on Earth at similar altitudes. Thus once condensation starts a Martian  $\text{CO}_2$  cloud will have about 1000 times the mass of a terrestrial cirrus cloud. Given an equal number of nuclei, the particle radius of Martian clouds will be about 10 times larger than that of terrestrial cirrus particles, consistent with the results shown in Fig. 2.

The larger the particles, the fewer are needed to reduce the saturation ratio to one. Figure 2 also shows the maximum particle concentration ( $N_{\text{max}}$ ) for three contact parameters as a function of cooling rate. For cooling rates above about 100 K/day, all of the available  $\text{CO}_2$  vapor condenses out (thus flattening the curves for  $m = 0.90$  and  $m = 0.95$ ). For the case in which the contact parameter is  $m = 0.99$ , cooling rates above about 100 K/day allow much smaller dust particles, on the order of the assumed dust distribution mean radius ( $r_o = 1.0\text{ }\mu\text{m}$ ), to nucleate. The limiting factor in this case was not only the total amount of  $\text{CO}_2$  vapor available, but also the total number of particles available for nucleation.

The temperature at which the nucleation rate is  $1\text{ sec}^{-1}\text{ cm}^{-3}$  for a number of particle sizes at a constant contact parameter is shown in Figure 3. It can be seen that, for smaller particles to achieve the same nucleation rate, colder temperatures are required. Several temperature profiles are also shown in Figure 3, including the temperature profile measured during the Mars Pathfinder entry. It has been speculated that carbon dioxide clouds may form at the coldest temperatures measured in the Pathfinder data set, near 80 km (Clancy and Sandor, 1998). This idea is consistent with our model calculations as long as there are nucleating particles available at these altitudes with radii of least  $r = 0.5\text{ }\mu\text{m}$  (for nucleation rates of  $J = 1\text{ sec}^{-1}\text{ cm}^{-3}$ ). However, such large particles will fall out from the atmosphere quickly. For example, a particle with a radius  $r = 0.1\text{ }\mu\text{m}$  will fall approximately 10 km in 10 minutes at altitudes near 80 km. Hence it seems unlikely that  $\text{CO}_2$  clouds would form under the Mars Pathfinder conditions unless even lower temperatures occurred previously to the measurements. Also shown in Figure 3 is the curve where the saturation ratio,  $s$ , is equal to one. Evaporation will occur to the right of the  $s = 1$  curve, and to the left,  $\text{CO}_2$  vapor will condense.

### 3.0 Condensation

After nucleation occurs, condensation controls the further growth of ice particles. The application of some terrestrial particle growth models to this problem is inappropriate because of the different diffusion regime that exists for a cloud particle condensing out of the atmosphere's primary gaseous constituent. The transfer of mass and energy between the particle and its surroundings dictates the rate of condensation and conversely evaporation. The theoretical treatment of these processes must represent a continuous transition through all Knudsen numbers. The Knudsen number is defined as  $Kn = \lambda/2r_d$ , where  $\lambda$  is the mean free path of the continuum gas and  $r_d$  is the particle radius. Terrestrial cloud particle growth generally concerns itself with the continuum regime when the mean free path of the continuum gas is small with respect to the condensing particle. This regime is frequently referred to as the diffusion regime since the diffusion rate of the condensing vapor ultimately limits the growth rate. When the mean free path is on the order of the particle size or larger then there is a transition to a regime in which the particle may be treated like a molecule in kinetic theory. This regime is called the kinetic regime and the transfer processes are then controlled by the kinetic properties of the condensing vapor. The transition from the diffusion regime to the kinetic regime depends on the pressure of the major gas. At a distance of approximately one mean free path from the condensing particle, there is a pressure jump that represents the discontinuity between the condensed surface and the ambient atmosphere. Within this distance, defined as the Knudsen layer, the growth is always in the kinetic regime. Beyond this distance, in the continuum region, the condensing vapor will be diffusion limited.

Several models of particle condensation and evaporation have been developed which demonstrate the behavior described above. A model developed by Toon et al. (1989) is described in detail below. While this particular model has been widely used by the terrestrial community for applications that reside within the diffusion regime, it is applicable across all Knudsen numbers.

An approximate growth rate of a particle due to condensation is (Toon et al. 1989)

$$d\dot{r}/dt = g_0 n_{vap} [(S+1) - A_k (1 + g_1 g_2 Q_{rad})] / [1 + g_1 g_0 n_{\infty}] \quad 3.1$$

In this expression  $n_{vap}$  is the vapor pressure of the condensing vapor and  $n_s$  is the number density of condensing molecules in the gas phase infinitely far from the particle.  $A_k$  is the Kelvin correction that accounts for the effects of particle curvature on the vapor pressure.  $Q_{rad}$  is the radiative heating rate of the particle (which we have assumed is zero in this work). The terms  $g_0$ ,  $g_1$  and  $g_2$  are growth kernels that contain the dependencies of the condensation growth on the vapor diffusion, effects of sedimentation on the flux of mass to the particle, and the latent heat of condensation:

$$g_0 = D' F_v M / \rho A \quad 3.2$$

$$g_1 = L_c^2 M \rho r / RT^2 K' F_i \quad 3.3$$

$$g_2 = 1/L_e 4\pi r^2 \rho \quad 3.4$$

$M$  is the molecular weight of the condensing gas and  $A$  is Avagadro's number ( $r$  and  $\rho$  have the same meaning as above).  $F_v$  and  $F_t$  are ventilation corrections that account for the effects of sedimentation on the flux of condensing vapor and heat to and from the particles.  $L_e$  is the latent heat of sublimation and  $T$  is the temperature. In these expressions,  $D'$  and  $K'$ , are the diffusion and the thermal conduction coefficients respectively:

$$\begin{aligned} D' &= DC / (r + f_c CK n_d / \phi_o) \\ K' &= KC / (r + f_t CK n_t / \phi_o) \end{aligned} \quad 3.5$$

$D$  is the diffusivity of the condensing vapor,  $K$  is the thermal conductivity of the continuum gas, and  $C$  is the capacitance of the particles that corrects for the effects of particle shape on the condensation rate (Pruppacher and Klett, 1978). The Knudsen numbers are defined as above with the subscript  $d$  and  $t$  referring to the diffusive and thermal mean free paths respectively. Lastly,

$$\begin{aligned} f_c &= (1.33 + 0.71/Kn_d) / (1 + 1/Kn_d) + 1.33(1 - \alpha_a) / \alpha_a \\ f_t &= (1.33 + 0.71/Kn_t) / (1 + 1/Kn_t) + 1.33(1 - \alpha_c) / \alpha_c \end{aligned} \quad 3.6$$

Here  $\alpha_a$  is the sticking coefficient (assumed to be unity) and  $\alpha_c$  is the thermal accommodation coefficient (assumed to be unity).  $Kn_d$  and  $Kn_t$  are the diffusive and thermal Knudsen numbers respectively and are defined by

$$\begin{aligned} Kn_d &= 3D' / (vr) \\ Kn_t &= 3K' / [\rho v (C_p - 0.5R)r] \end{aligned} \quad 3.7$$

where  $v$  is the mean thermal velocity and  $C_p$  is the heat capacity of the air.

The transition between the kinetic and diffusion regimes can be seen in Eq. 3.5. As the Knudsen number increases, either by reducing the condensing particle size or by increasing the mean free path, the effective diffusion coefficient is reduced. Figure 4 shows the condensation growth rate for a constant supersaturation of 20% as a function of Knudsen number (or atmospheric pressure) for two particle sizes. Also shown in Figure 4 is the approximate point at which the transition between diffusion control to kinetic control occurs. Present Martian pressures at cloud forming altitudes reside in the  $0.1 \times 10^{-3}$  bar range that places the condensation in the kinetic control regime. Early Mars cloud formation might have occurred at pressures of around 0.1 bars. At these pressures the growth mechanism is transitioning from the kinetic regime into the diffusion regime.

The amount of inert gas in the continuum also modifies the condensation growth rate by effecting the diffusion rate coefficient. The binary diffusion rate coefficient can be written as

$$D = (n_1 \lambda_1 v_1 + n_2 \lambda_2 v_2) / (n_1 v_1 + n_2 v_2) \quad 3.8$$

where  $n$  is the gas number density,  $\lambda$  is a mean free path, and  $v$  is the thermal molecular velocity:

$$\begin{aligned} \lambda_{1,2} &= 2\eta_{1,2} / \rho_{1,2} \\ v_{1,2} &= \sqrt{2kT/m_{1,2}} \end{aligned} \quad 3.9$$

The subscripts refer to the two molecular species respectively. In the limit of one species being absent (e.g.,  $n_2 = 0$ ) then Eq. 3.8 reduces to the coefficient of self diffusion

$$D_s = 2\eta / \rho \quad 3.10$$

where  $\eta$  is the molecular viscosity and  $\rho$  the air density. Changes in the diffusion coefficient associated with changes in the fraction of inert gas can account for a 200% change in the actual condensation growth rate. In addition to an overall decrease in the growth rate at all Knudsen numbers, an increase in inert gas shifts the transition from kinetic to diffusion regimes toward higher Knudsen numbers. The current Martian inert gas fraction is approximately 5%, composed mostly of nitrogen. If the nitrogen abundance in the early Martian atmosphere was comparable to current Mars CO<sub>2</sub> amounts, then the fraction of inert gas may have been as low as 1%.

The rate of growth also depends on the amount of supersaturation (Eq. 3.1). Glandorf et al. (this issue) were able to measure the growth rate of CO<sub>2</sub> ice as a function of supersaturation in the laboratory. Figure 5 shows the condensational growth rate on a flat surface in units of grams per second. The laboratory data from Glandorf et al. (this issue) are plotted as open squares. In the experiments of Glandorf et al. (this issue) the CO<sub>2</sub> ice was grown onto a thin 2 cm diameter silicon wafer pre-coated with a thin (~ 1  $\mu$ m thick) layer of water ice. Based on the absorption of infrared light through the wafer the total thickness of CO<sub>2</sub> ice was determined. Over plotted in Figure 5 are the calculated growth rates using the model described here (dashed line) and another developed by Young (1993) (solid line). Woods (1999) pointed out that crystal surface kinetics could impede the growth of ice crystals depending on the efficiency of molecular absorption, surface diffusion and transfer of molecules into the crystal lattice. These properties may lead to a growth barrier that limits the size of CO<sub>2</sub> ice crystals. However, the good agreement the theories presented here have with the data suggests that the growth of CO<sub>2</sub> is limited only by the rate of diffusion of CO<sub>2</sub> gas to the condensing surface ice with little or no activation barrier.

The growth rate of a particle will change as the growth regime changes from kinetic to diffusion control. The time it takes for the particle to grow from a radius  $r' = 0$  to  $r' = r$ , assuming a uniform sphere, can be approximated from Eq. 3.1. In the Diffusion limit, Knudsen numbers are small and the dominant term in Eq. 3.1 is  $g_o$ , which is proportional to  $r^{-1}$ , and the growth time is approximately

$$\tau_g = \int \frac{dr}{g_o} \propto r^2 \quad 3.11$$

If, however, the particle is growing in the kinetic limit, the Knudsen numbers will be large and  $g_o$  independent of  $r$ . In the kinetic regime the growth time becomes

$$\tau_g \approx \frac{r}{g_o} n_{vap} (S - 1) \propto r. \quad 3.12$$

Figure 6 shows the growth time as a function of particle radius and the time it would take a particle of the same radius to fall 1 km. Indicated in Figure 6 is the point at which the growth rate changes from diffusion to kinetic control. The slope of the growth time changes from that of nearly directly proportional to the particle radius in the kinetic limit (Eq. 3.11) to that of the square of the particle radius in the diffusion limit (Eq. 3.12). The time it takes a one  $1 \mu\text{m}$  sized particle to grow to  $10 \mu\text{m}$  is approximately  $\tau_g = 0.1$  sec, while the fall time for the same particle is on order hours. Hence, one expects particle sizes larger than  $10 \mu\text{m}$ . Conversely, an evaporating  $1000 \mu\text{m}$  particle would last for several hours while falling at a rate of about  $1 \text{ km min}^{-1}$ .

#### 4.0 High Altitude CO<sub>2</sub> Clouds

The coldest temperatures yet observed on Mars were those measured near 80 km during the Mars Pathfinder entry (see Figure 3). These cold temperatures are believed to be the result of vertically propagating thermal tides (Haberle et al. 1999; Magalhaes et al. 1999). Temperatures in this region, as low as 85 K, dipped below the vapor pressure curve of CO<sub>2</sub> suggesting that carbon dioxide could condense here. In Mariner 9 and Viking limb observations high altitude hazes have been identified at altitudes between 60 and 90 km (Jaquin 1986). Pre-dawn observations of blue clouds by the Mars Pathfinder lander have been speculated to be high altitude CO<sub>2</sub> clouds (Clancy and Sandor, 1998). Assuming that the color of these clouds is a result of their size, Clancy and Sandor (1998) estimated that these clouds contain small particles with radii less than  $0.3 \mu\text{m}$ . To study the possible formation of high altitude carbon dioxide clouds several simulations were conducted. In each simulation the temperature was lowered and then raised by an equal amount at a specified altitude. The period of the temperature deviation, based on the approximate frequency of a propagating thermal wave (Haberle et al., 1999), was equal to 3 hours. The magnitude of the temperature deviation was taken from the Mars Pathfinder entry profile such that the minimum temperature achieved was approximately equal to 85 K. Based on a background temperature of 105 K, this simulated thermal wave results in a cooling rate of approximately 6.5 K per hour or 160 K per day.

The largest constraint on the formation of clouds at these high altitudes is the availability of nuclei, assumed in these simulations to be dust. For the first simulation we assumed an initial dust mixing ratio that is constant in height that results in a visible surface optical depth of  $\tau = 0.3$ . This initial distribution is allowed to evolve over time through sedimentation. While supersaturations of greater than 35% were achieved, no clouds formed. The reason for the lack of cloud formation is that, at these altitudes greater than 60 km, dust particles larger than  $0.1 \mu\text{m}$  fall out so quickly (on order of an hour) there are no nucleation sites for clouds to form upon. Possibly there is a flux of dust into the region. The second simulation assumes there is a flux of dust from above equal to  $5 \text{ particles cm}^{-3} \text{ sec}^{-1}$  with a log-normal distribution ( $r_o = 0.1 \mu\text{m}$ ,  $\sigma = 2.0$ ). This downward flux may be the result coagulating meteoritic dust (Michelangeli 1993) or the result of the enhanced vertical mixing from below at another location followed by decent into the region of interest, associated with dust storms (Murphy et al. 1995). The increase in dust at high altitudes correspondingly increases the surface visible optical depth to  $\tau = 0.8$ . Under these conditions there are sufficiently large dust particles ( $\sim 0.5 \mu\text{m}$ ) at high altitude for nucleation to occur and a cloud forms. Figure 7 shows the effective cloud particle radius and cloud mass mixing ratio as a function of altitude for this simulation. The cloud particles grow to an effective radius of  $10 \mu\text{m}$  quickly after nucleating. These cloud particles fall out quickly and evaporate in the sub-saturated layers below. The mass mixing ratio reaches approximately 35% (indicated by the dashed line in the right panel in Figure 7) of the mass of the atmosphere reflecting the supersaturation required for nucleation. The maximum concentration of cloud particles is never greater than approximately  $0.001 \text{ cm}^{-3}$ . The integrated optical depth across the cloud is approximately  $\tau = 0.001$  at a  $\lambda = 0.64 \mu\text{m}$  making it very unlikely that this cloud could be visible from the surface. If viewed across the limb the additional path length would increase this optical depth making it possible that it could be observed as a thin haze like those identified in Viking images (Jaquin 1986).

If the region of cooling were to occur at lower altitudes, larger cloud particles would form, as there is more mass to condense for the same amount of saturation. Figure 8 shows the effective cloud particle radius and mass mixing ratio for a cloud forming in the same way as described above, but at 60 km rather than at 80 km. Cloud particle effective radii at these altitudes are greater than  $500 \mu\text{m}$  in size. Because of their large size these cloud particles are able to fall further into the sub-saturated region below the cloud. As a result a much more vertically extensive cloud forms, spanning over 10 km before completely evaporating.

According to this study the temperatures seen near 80 km in the Mars Pathfinder entry profile are cold enough to nucleate  $\text{CO}_2$  particles if there are dust grains larger than about  $r = 0.5 \mu\text{m}$  available. Assuming there are particles large enough to nucleate, the cloud particles quickly grow due to the high critical supersaturation necessary to nucleate carbon dioxide ice. As these particles grow they fall very quickly into under saturated regions and evaporate. The simulations done here suggest that, while carbon dioxide particles may form at these altitudes, they will be large ( $r_{eff} > 3 \mu\text{m}$ ) and at very small concentrations ( $N_{max} \sim 0.01 \text{ cm}^{-3}$ ). The end result would be a "snow" flurry of  $\text{CO}_2$  rather

than sustained "blue" clouds with any appreciable optical depth. At lower altitudes (and hence greater CO<sub>2</sub> pressures), the carbon dioxide cloud particles are even larger ( $r_{eff} > 500 \mu\text{m}$ ) and at concentrations that, depending on the cooling process, may result in optical depths greater than one. These particles also fall out quickly, but because of their large size, can penetrate further into the sub-saturated region below the cloud.

The physics of CO<sub>2</sub> cloud formation is rather simple. Since supersaturations greater than 30% (Glandorf et al., this issue) are needed to form particles, at least 30% of the atmospheric mass will condense when clouds form. Distributing this mass over even a relatively large number of nuclei will result in large particles. For instance, if 30% of the atmospheric mass were distributed over 100 particles per cm<sup>-3</sup> at 80 km altitude the average particle radius would be about 2  $\mu\text{m}$ , too large to explain the blue clouds following the method proposed by Clancy and Sandor (1998).

We conclude that CO<sub>2</sub> ice clouds may form near 80 km altitudes on Mars, given the Pathfinder entry profile. However, such clouds are unlikely to have the small particle sizes required by Clancy and Sandor (1998) to explain the Martian blue clouds. Rather it is more likely that the clouds, either carbon dioxide or low altitude water ice, act as neutral scatterers and simply reflect the sky color which, due to Rayleigh scattering is likely to be blue at these altitudes (Colaprete et al. 1998).

## 5.0 The Early Martian Atmosphere

Numerous geomorphologic features suggest that liquid water once flowed over the surface of Mars about 3.8 BYA (Carr, 1986, Pollack et al. 1987). Currently the mean surface temperature of Mars (212 K) is far too cold and the atmosphere too thin (6.2 mbar) for water to be stable at its surface for any length of time. Compounding the problem is the general acceptance that the early sun was less luminous than it is today. It is estimated that for the epoch of river network formation on Mars the sun was 25% less luminous (Gough 1981). Therefore, during this period in Mars' history it is supposed that a thick carbon dioxide atmosphere was required to provide enough greenhouse effect to warm the surface above the freezing point of water. Initial modeling indicated that as much as 5 bars of CO<sub>2</sub> would be required (Pollack et al. 1987). Figure 9 shows the temperature profile for a 2 bar CO<sub>2</sub> atmosphere at 75% present solar luminosity calculated by Pollack et al. (1987) using a standard radiative-convective model.

Additional consideration of the greenhouse model by Kasting (1991) identified a problem with the thick CO<sub>2</sub> atmosphere solution. At several bars of CO<sub>2</sub> pressure, the atmosphere becomes saturated with respect to CO<sub>2</sub> allowing for the formation of carbon dioxide clouds. Kasting (1991) assumed that the temperature profile in the region of cloud formation would necessarily follow the wet CO<sub>2</sub> lapse rate. This profile would lead to a warmer middle atmosphere and consequently a colder surface (Figure 9). Furthermore, if carbon dioxide clouds did form, a "run away condensation" effect may occur such that any more carbon dioxide added to the atmosphere would condense out. This effect would limit the total carbon dioxide pressure available for greenhouse warming. Kasting

(1991) estimated for solar luminosity of 70% current values that the pressure at which this "run away" condensation occurs is approximately 1.5 bars. At this pressure or higher the entire Martian troposphere would be saturated and the surface temperature would be a chilly 214 K. By comparison, with CO<sub>2</sub> condensation neglected, Pollack et al. (1987) found solutions for the surface temperature of 273 K at 5 bars of CO<sub>2</sub>.

The conclusions of Kasting (1991) are based on thermodynamic arguments alone and do not take into consideration cloud optical properties. Carbon dioxide ice has very different optical properties than water ice. Having very little absorption at infrared wavelengths, CO<sub>2</sub> ice makes for an excellent scatterer. Recognizing this, Forget and Pierrehumbert (1997) demonstrated that the CO<sub>2</sub> clouds predicted in Kasting's models might actually provide additional warming through a scattering greenhouse effect. Forget and Pierrehumbert (1997) found that the magnitude of the effect depends greatly on cloud particle size, cloud optical depth, and surface coverage. For example, given a 2 bar CO<sub>2</sub> atmosphere and assuming a cloud particle radius of 10  $\mu\text{m}$ , a carbon dioxide cloud with optical depth of about 4 could warm the surface to the freezing point of water (Figure 9). For larger particles and higher optical depths the amount of warming increased. Using a similar model, Mischna et al. (2000) obtained similar results as Forget and Pierrehumbert (1997). Furthermore, Mischna et al. (2000) also demonstrated the effects of cloud altitude on the surface temperature. While high altitude (>15 km) clouds will warm the surface, lower altitude clouds, with the same particle characteristics, ultimately work to cool the surface of the planet. To determine the true effects that carbon dioxide clouds have on the environment, the characteristics of the clouds need to be interactively determined along with the temperature profile.

## **6.0 Model Description**

The inherent coupling between clouds and their environment requires that the microphysics, transport of particles and gases, thermal structure and the radiation field be solved for simultaneously. Therefore, for this work the cloud microphysical model described above is coupled to a two-stream radiative transfer model that includes both carbon dioxide and water vapor. Transport of gases, particles and potential temperature is handled by an eddy diffusion scheme in which the diffusion coefficients are calculated by a boundary layer turbulent mixing model. Both dust and cloud optical depths are solved for using stratified Mie theory, with the optical properties of CO<sub>2</sub> ice taken from Hansen (1997a, 1997b) and those of dust from Ockert-Bell (1997) for visible wavelengths and Clancy et al. (1998) for wavelengths in the infrared. The optical properties of the cloud particles require that the radiative properties of the atmosphere, including both absorption and scattering, be treated rigorously at all wavelengths in the solar and infrared. The next two sections will describe the boundary layer model and the radiative transfer model.

### **6.1 Boundary Layer Model**

The planetary boundary layer model follows that described by Haberle et al. (1993). It is a 1D surface-atmosphere model that solves the energy and momentum equations for the atmosphere and heat conduction at the surface. The turbulent eddy diffusion of

momentum  $K_m$  and heat  $K_h$  is derived from the second-order closure theory of Mellor and Yamada (1974). In this scheme, turbulent kinetic energy is calculated assuming a balance between production and dissipation. Above a critical value for the gradient Richardson number,  $Ri_c$ , all turbulence is extinguished. The Richardson number is defined as

$$Ri = \frac{\beta g \partial \theta / \partial z}{(\partial u / \partial z)^2} \quad 6.1.1$$

where  $\beta$  is the volume expansion coefficient,  $g$  is gravity,  $\theta$  is the potential temperature and  $u$  is the wind speed. The variation of the wind speed with height is not modeled here, instead a constant vertical wind gradient of  $5 \text{ m sec}^{-1}$  in  $1 \text{ km}$  is assumed (Haberle et al. 1993). The eddy mixing coefficients are based on functions derived by Arya et al. (1988). The surface heat flux is applied at the surface-atmosphere boundary as a transfer of sensible heat between the surface and the lowest atmospheric layer. The eddy coefficients are added to a background coefficient, which is equal to  $k_o = 10^2 \text{ cm}^2 \text{ sec}^{-1}$  at the surface and increases with altitude as the inverse of the square root of air density.

## 6.2 Radiative Transfer Model

To understand the radiative effect these clouds have on their environment, the atmospheric heating and cooling rates must be accurately determined. These heating and cooling rates must be calculated over the range of contributing absorber amounts and their vertical distributions. Line-by-line calculations are computationally expensive due to the large number ( $\sim 10^5$ ) of spectral lines of the principle absorbing gases ( $\text{CO}_2$  and  $\text{H}_2\text{O}$ ) and the large effects that pressure broadening has on the spectral line absorption coefficients and thus on the vertical homogeneity of the atmosphere. One alternate approach that is computationally efficient and still accurate is the correlated- $k$  method. The correlated- $k$  method is an approximate technique for the accelerated calculation of fluxes and cooling rates for inhomogeneous atmospheres. This method is capable of achieving an accuracy comparable with that of line-by-line models with an extreme reduction in the number of radiative transfer operations performed. The radiative transfer operations for a given homogeneous layer and spectral band are carried out using a small set of absorption coefficients that are representative of the absorption coefficients for all frequencies in the band (Lacis and Oinas, 1991).

Since the spectral absorption coefficient  $k(\nu)$  is a highly repetitive function of wavenumber, computational efficiency can be improved by replacing integration over wavenumber with a regrouping by ascending order of the absorption coefficients. A characteristic value can then be specified for any segment of the new function. Mathematically, this is accomplished by mapping the absorption coefficients  $k(\nu)$  from spectral space to a space defined by a variable  $g$ , where  $g(k)$  is the fraction of the absorption coefficients,  $k_i$ , in a set smaller than  $k(\nu)$ . The function  $g(k)$  is often referred to as the cumulative probability function. For the simulations done here, gaseous absorption is calculated over 55 spectral bands that span from  $40 \text{ cm}^{-1}$  to  $30000 \text{ cm}^{-1}$ . At wavenumbers above  $15000 \text{ cm}^{-1}$  only dust is considered an active absorber in the Martian

atmosphere. Table 6.1 shows the spectral bands used and the key absorbing species within each band. A spectral band is divided into 8 subintervals in  $g$  space chosen to have half Gauss-Legendre spacing. The absorption coefficients for carbon dioxide and water vapor and their weights were provided by Bob Haberle (1998, personal communication).

In the calculation of optical depths for a spectral band the atmospheric parameters upon which  $k$  is dependent must be taken into account. For each gas species, the dependence on pressure and temperature is addressed by obtaining and storing values of  $k$  on a grid that has spacing fine enough to allow linear interpolation to accurately approximate  $k$  for a general atmosphere. The reference  $k$  values are stored over 11 pressure levels ranging from 0.1 mbar to 10 bars and 7 temperature levels ranging from 50 - 350 K.

For an absorber amount  $u$ , the spectrally averaged gas transmissions are expanded in terms of an exponential sum of the form

$$T(u) = \sum_{i=1}^N g_i e^{-k_i u} \quad 6.2.1$$

Each exponential term,  $k_i$  acts as an equivalent absorption coefficient. To calculate the irradiance for one gas in each spectral band,  $N$  monochromatic radiative transfer calculations are performed, one for each  $k_i$  term (Sun and Rikus 1999, Lacis and Oinas 1991, Mlawer et al. 1997). Under conditions such that the mapping  $v \rightarrow g$  is identical for adjacent layers, that is, the  $k$  distribution at a given altitude is fully correlated in spectral space with the  $k$  distribution at all altitudes, this method is exact for inhomogeneous atmospheres. However, as pressure, temperature and relative molecular concentration change from one altitude to another, each  $k_i$  value will be affected differently. For example, overlapping absorption lines of different strengths and large-scale shifts in line strength distribution within hot band regions can produce spectrally uncorrelated changes in the  $k$  distribution (Lacis and Oinas, 1991).

To evaluate the combined transmission for overlapping gases it is normally assumed that the absorption spectral lines from the two gases are randomly distributed over a spectral band. Under these conditions the mean transmissions of the gas mixture can be calculated by the double sum,

$$T(u_1, u_2) = \sum_{i=1}^N g_i e^{-k_i u_1} \sum_{j=1}^N g_j e^{-k_j u_2} \quad 6.2.2$$

where  $u_1$  and  $u_2$  are the absorber column amounts of the two gases. Although one can solve the problem of overlapping gaseous absorption, the number of monochromatic calculations increases to the product  $N_1 N_2$ . To reduce the number of calculations required, an additional interpolation variable, the binary species parameter  $\eta$  can be defined (Mlawer et al. 1997, Sun and Rikus 1999):

$$\eta = \frac{u_1}{u_1 + fu_2} \quad 6.2.3$$

where  $f$  is the ratio of the respective integrated line strengths of the two species  $u_1$  and  $u_2$ . Parameter  $f$  represents the relative radiative importance of the two absorbing gases. A value of  $\eta$  near zero implies that the species  $u_2$  is radiatively dominant, whereas a value near 1 indicates that the species  $u_1$  is dominant.

We follow the approach developed by Mlawer et al. (1997) for the Earth's atmosphere. Twenty reference values of the binary species parameter are used for interpolation. The first ten reference values are spaced evenly from  $10^{-6}$  to  $10^{-1}$ ; the next ten reference values are space evenly from  $10^{-1}$  to 1.0. At each reference value of pressure, temperature and binary species parameter, a weighted absorption coefficient is obtained for each optical depth at each of 64 subintervals according to the relation

$$k_w(g_1, g_2) = \eta k_1 + (1 - \eta)k_2. \quad 6.2.4$$

The calculated effective absorption coefficients are sorted in ascending order and the final absorption coefficient is obtained by averaging the  $k(g)$  values in each of the 8 subintervals (Mlawer et al., 1997). The transmission may then be rewritten as

$$T(u_1, u_2) = \sum_{i=1}^N g_i e^{-k_{eff,i} u_{mix}} \quad 6.2.5$$

where  $u_{mix}$  is the effective column amount for each layer defined by

$$u_{mix} = u_1 + fu_2 \quad 6.2.6$$

and  $f$  is defined as before. The optical depth of the mixture of gases is just the product of the column mixture amount,  $u_{mix}$ , and the effective absorption coefficient,  $k_{eff}$ . To assess the validity of this approximation, the transmission calculated by Eq. 6.2.2 can be compared to those calculated using Eq. 6.2.5 for different values of the binary species parameter. Figure 10 shows the fractional percent difference in the transmission ( $=100 \times (T_1 - T_2)/T_1$ ) calculated using Eq. 6.2.2 and Eq. 6.2.5 for several values of  $\eta$  within a spectral region ( $\nu = 3580 \text{ cm}^{-1}$ ) that contains both  $\text{H}_2\text{O}$  and  $\text{CO}_2$  absorption. As shown in Table 5.1 the line strength of water dominates that of  $\text{CO}_2$  within the  $3580 \text{ cm}^{-1}$  band. Assuming uniform mixing at all altitudes, the agreement between the two methods is good. For values of the binary species parameter greater than  $\eta = 0.1$ , the maximum difference in transmissions for the true and the effective coefficients was never greater than about 2%. At values of  $\eta < 0.1$  water vapor becomes the major gas in the atmosphere and errors in this technique increase to between 5 and 10%. In the studies done here water vapor concentrations are never large enough to decrease  $\eta$  below 0.95.

The contribution of the water vapor self-continuum between 850 - 1200  $\text{cm}^{-1}$  is included by a separate procedure (Thomas and Nordstrom, 1985). The absorption coefficient is calculated from the relation

$$k_{H_2O} = \frac{p_{H_2O}^2}{RT} C_s \quad 6.2.7$$

where  $p_{H_2O}$  is the partial pressure of water vapor,  $R$  the gas constant, and  $T$  is temperature. The parameter  $C_s$  incorporates the temperature and frequency dependence of the absorption coefficient:

$$\begin{aligned} C_s &= C_v C_T \\ C_v &= 1.25 \times 10^{-22} + 1.67 \times 10^{-19} \text{Exp}[-2.62 \times 10^{-13} \nu] \\ C_T &= \text{Exp}\left[1800\left(\frac{1}{T} - \frac{1}{296}\right)\right] \end{aligned} \quad 6.2.8$$

Since the self-continuum absorption coefficient  $k_{H_2O}$  is approximately monochromatic across each spectrum band, a single  $k_{H_2O}$  is computed for each subinterval of  $g$  (Mlawer et al. 1997). Temperature and partial pressure dependence of the water vapor self-continuum is accounted for at each reference temperature and pressure as described above. For the simulations done here the water vapor profile assumed a constant relative humidity of 50% or 100% (see section 7.4). The effect of pressure-induced absorption by  $\text{CO}_2$  was included in the opacity calculations using the parameterization described by Kasting et al. (1984b).

For each subinterval in each band, a layer-by-layer radiative transfer calculation is performed. This treats each subinterval, which corresponds to a large number of frequencies in the band, in the same manner that a single spectral point is treated in a line-by-line model. Therefore, the treatment of absorption by the correlated-k method is entirely consistent with any two-stream radiative transfer algorithms. For this application we have used the rapid two-stream radiative transfer model for inhomogeneous multiple-scattering atmospheres developed by Toon et al. (1989). The atmosphere is divided into 60 layers, each 1.5 km thick.

For atmospheres with surface pressures greater than about 0.5 bar the amount of atmosphere that exists above the top of these 60 levels is substantial and needs to be accounted for. Adding one additional isothermal layer to the top of the model does this. This additional layer provides the down-welling infrared flux that would otherwise exist if the model extended to higher altitudes.

## 7.0 Model Results

Numerous simulations were conducted over a range of parameter space that included changes to the dust column, water vapor content, and  $\text{CO}_2$  abundance. Table 7.1 lists

parameters that were assumed in the simulations presented below. Some of these parameters, such as surface albedo, were assumed to be constant for all simulations. Where more than one value for a parameter appears, it indicates that this parameter was varied in sensitivity studies.

The first simulation results presented are directed at understanding the net radiative forcing of carbon dioxide clouds as a function of particle size and optical depth. The radiative forcing for the top of the atmosphere (TOA) and the surface (SFC) are defined as

$$\begin{aligned}\Delta F_{TOA} &= -(F_{S+IR}(\uparrow_{TOA}, cloudy) - F_{S+IR}(\uparrow_{TOA}, clear)) \\ \Delta F_{SFC} &= (F_{S+IR}(\downarrow_{SFC}, cloudy) - F_{S+IR}(\downarrow_{SFC}, clear))\end{aligned}\tag{7.0.1}$$

where  $\uparrow$  and  $\downarrow$  indicate up-welling and down-welling fluxes respectively. A negative forcing value typically means there will be a net cooling, while a positive value indicates there will be warming.

## 7.1 Cloud Forcing

To study the radiative forcing of CO<sub>2</sub> clouds, in a fashion similar to the work of Forget and Pierrehumbert (1997), stationary clouds consisting of particles with a single radius are inserted at 17 km and the radiative forcing calculated for a range of cloud optical depths. These calculations were done in a dust free atmosphere to be consistent with similar studies done previously (Forget and Pierrehumbert 1997; Mischna et al. 2000). Figure 11 shows the results of this study. Consistent with past studies, for particle sizes with radii greater than about 5  $\mu\text{m}$ , there is a positive radiative forcing at the top of the atmosphere (TOA) and the surface (SFC). This forcing reaches a maximum at optical depths of  $\tau = 10$  (at  $\lambda = 10 \mu\text{m}$ ). For optical depth greater than  $\tau = 10$  the surface forcing decreases becoming negative for optical depths greater than about  $\tau = 40$ . As the cloud becomes increasingly thick, its albedo rises until more solar flux is reflected above the cloud than infrared flux is trapped below. Mischna et al. (2000) found similar results in their work.

A different radiative forcing is seen above the cloud. While the TOA forcing decreases slightly for optical depths greater than  $\tau = 10$ , for optical depths greater than  $\tau = 100$  it approaches a constant value of approximately 30 W m<sup>2</sup>. The different forcing behavior above and below the cloud is the result of relative changes in radiative solar and IR fluxes above and below the cloud.

In the microphysical simulations done here, for an atmosphere containing 2 bars of CO<sub>2</sub>, clouds tend to form near 25 km rather than at 17 km. Therefore, in the following discussion the radiative forcing of a CO<sub>2</sub> cloud at altitudes near 25 km is considered. Figure 12 shows the up and down welling solar and IR fluxes for clear sky conditions and for a CO<sub>2</sub> cloud centered at 25.5 km with an optical depth  $\tau = 10$  ( $\lambda = 10 \mu\text{m}$ ). The decrease in incoming solar flux (due to the increase in the cloud's albedo) does not

compensate for the decrease in outgoing infrared flux (due to trapping below the cloud). Therefore, the total outgoing flux (solar + IR) above the cloud is always less for cloudy conditions than for clear conditions. This leads to a net warming above the cloud. These results represent an instantaneous snapshot of the radiative forcing in an atmosphere out of radiative equilibrium with the cloud. Therefore, these forcings will diminish as the atmospheric thermal structure evolves, in the absence of any other forcing or changes in cloud properties, until they are zero and the atmosphere is in radiative-convective equilibrium with the cloud.

Positive forcing above the cloud will warm the atmosphere at higher altitudes, which in turn, will eventually lead to warmer temperatures below. However, there are different response times associated with surface and atmosphere forcing. The response of the surface temperature to the negative surface forcing is almost immediate while the response to the positive warming above the cloud will occur on the radiative time scale of the atmosphere. For a 2 bar atmosphere this radiative time scale is on order years. The time scale at which the cloud itself is evolving via particle sedimentation and latent heating is on order hours. Thus while the cloud radiative forcing may lead to a positive global forcing, the rate at which it does so is substantially less than the rate at which the cloud changes. Furthermore, as the atmosphere does warm through radiative forcing, the cloud will thin and lose its radiative impact. The net result of the cloud is to stabilize the atmosphere, and in doing so, partially eliminate itself. Therefore, the results of previous studies (Forget and Pierrehumbert 1997; Mischna et al. 2000) do not accurately portray an atmosphere in equilibrium. Such stabilization is illustrated in Mischna et al.'s Fig. 3 in which the evolved atmosphere is too warm to support cloud formation.

## 7.2 Cloud Formation

The next series of simulations allows clouds to evolve. The temperature profile is initially defined by selecting a surface temperature and following the dry adiabatic lapse rate upward until the vapor pressure of  $\text{CO}_2$  is reached. At this point the temperature curve follows just above the vapor curve so that the atmosphere is 1% unsaturated throughout the region where Kasting (1991) predicts clouds to form. When the temperature reaches an initial skin temperature, the profile becomes isothermal. In this initial state the atmosphere is cloud free and warmer than the standard radiative-convective solution. As time passes the atmosphere cools leading to cloud formation.

Figure 13 shows several temperature profiles for a typical simulation that assumed 2 bars of carbon dioxide, a water vapor relative humidity of 50% and dust radiative effects set to zero. Shown in Figure 13 are the  $\text{CO}_2$  saturation temperature profile (dash-dot line) and the temperature profile for a cloud free case (dashed line). Where the cloud free temperature profile falls to the left of the saturation profile,  $\text{CO}_2$  clouds may form. When the  $\text{CO}_2$  clouds form, the release of latent heat brings the atmosphere temperature to the saturation temperature. The solid line shows the resulting temperature profile with  $\text{CO}_2$  clouds.

Martian carbon dioxide clouds follow a cycle of formation and loss with a frequency on order of days (depending on transport time scales). Clouds initially form at the tropopause where temperatures first dip below the CO<sub>2</sub> saturation temperature. The cloud particles are very large and, with average radii  $\sim 1000 \mu\text{m}$ , they fall into sub-saturated regions and evaporate in about a day. As the clouds fall they carry with them the dust they nucleated onto and quickly remove dust from the region of cloud formation. This, combined with the fact that latent heating from cloud condensation has warmed the atmosphere, makes the continued presence of a cloud within this region difficult. It isn't until fresh dust is mixed in and/or the atmospheric temperatures cool that cloud formation can occur again.

This atmospheric heating is the principle difficulty associated with warming the surface via a scattering carbon dioxide cloud. Clouds of the appropriate optical thickness and altitude never last longer than several days. There are periods of surface warming while clouds are present, however, the induced local radiative warming, combined with latent heating, eliminates the clouds. Furthermore, surface warming is partially compensated by the increase in outgoing infrared flux from the warmer middle atmosphere (between 10 - 40 km). Several other factors affect the total amount of warming that these clouds can provide, including the presence of atmospheric dust, the abundance of water vapor and the total atmospheric pressure. In the following sections several sensitivity tests are used to determine the effect of these factors on the total surface warming of carbon dioxide clouds.

### 7.2.1 Atmospheric Dust

It is unclear how much aerosol, or even what type, may have been present in the early Martian atmosphere. If Mars was wetter early in its history than now, wet deposition may have reduced the amount of atmospheric dust below what is currently seen in the Martian atmosphere. However, with a thicker atmosphere, the residence lifetime of atmospheric dust would be substantially longer. The fall time for a  $1 \mu\text{m}$  dust particle in a 2 bar atmosphere is  $\sim 100$  times longer than in the current Martian atmosphere. Furthermore, dust lifting, which goes as the product of the air density and the wind velocity squared, would more efficient for a thick CO<sub>2</sub> atmosphere. If the dust is acting as nucleating sites, its distribution will have significant effects on cloud formation. However, any dust in the atmosphere will also have a direct effect on the radiative forcing of an existing CO<sub>2</sub> cloud. Figure 14 shows the radiative forcing for a stationary cloud at 17 km with  $50 \mu\text{m}$  particles with and without atmospheric dust. The effect of a strongly IR absorbing aerosol, such as mineral dust, is to reduce the magnitude of the forcing by decreasing the planetary albedo. The presence of dust also acts to warm the middle atmosphere (10 - 40 km) through absorption of solar radiation, which leads to an over all reduction in the total cloud cover. Neither Forget and Pierrehumbert (1997) or Mischna et al. (2000) include the radiative effects of dust in their simulations.

Dust readily absorbs scattered infrared flux that would otherwise find its way to the surface in the dust free simulations. Therefore, while there is still a net infrared flux trapped below the cloud, a significant fraction of it goes to warming the dust in the

atmosphere below the cloud rather than the surface. For the simulations that included dust, the initial atmospheric dust column was defined to have a log-normal distribution with a modal radius of  $1.0\ \mu\text{m}$ , a standard deviation of  $\sigma = 1.8$  and an initial scale height of  $15\ \text{km}$ . The surface dust concentration was initially  $10\ \text{cm}^{-3}$  giving an optical depth in the visible ( $\lambda = 0.65\ \mu\text{m}$ ) of  $\tau = 0.25$  at the surface. A relative humidity of 50% was assumed for these two simulations. The results of the dust free simulation (Figure 13) are similar to those of Forget and Pierrehumbert (1997) and Mischna et al. (2000).

Figure 15 shows the cloud surface optical depth as a function of time smoothed over a 5 day window. When dust is included there is a reduction in the average cloud optical depth as well as the fraction of time a cloud is present. In the dust free simulation the average optical depth is approximately  $\tau = 3.0$ , while in the simulation with dust included the average cloud optical depth is reduced to approximately  $\tau = 1.0$ . In the dust free simulation a cloud with an optical depth greater  $\tau = 0.1$  than was present 52% of the time, compared to 40% of the time for the simulation that included dust. The total number of clouds with optical depths greater than  $\tau = 5$  was also significantly less for the dusty simulation compared to the dust free simulation. Figure 16 shows the surface temperature as a function of time for the dusty and dust free cases. In general, when dust is included in the simulation the average cloud optical depth and the total time a cloud is present is less, leading to slightly lower surface temperatures. This effect is due to an overall reduction in the albedo of the atmosphere allowing more solar radiation to be absorbed before it reaches the ground as well as an overall reduction in the presence of clouds due to a warmer middle atmosphere.

### 7.2.2 Water Vapor

Water vapor is an excellent absorber in the infrared making its role in the radiative balance very important in two ways. First, water vapor provides substantial greenhouse warming above an otherwise dry  $\text{CO}_2$  atmosphere. Absorption in the near and far infrared spectrum that is otherwise absent of any strong carbon dioxide absorption, can provide substantial surface warming depending on the total concentration and distribution within the atmosphere. For example, water with a constant relative humidity of 50%, provides an approximate 10 K of surface warming due to water vapor greenhouse relative to a dry atmosphere with a  $\text{CO}_2$  surface pressure of 2 bars. Secondly, water vapor, in the same fashion as dust, acts to dampen the total radiative forcing generated by a scattering carbon dioxide cloud by absorbing the downwelling infrared light scattered by  $\text{CO}_2$  clouds. The warming from the water vapor greenhouse ultimately reduces the total frequency and optical depth of  $\text{CO}_2$  clouds and hence their ability to warm the surface.

To understand the relative importance of water vapor abundance to the warming ability of  $\text{CO}_2$  clouds, two simulations were conducted. In these simulations the relative humidity was set to a constant 50% and 100% respectively and the radiative effects of dust were set to zero. Figure 17 shows the surface temperature as a function of time for these two simulations. As the relative humidity is increased the amount of greenhouse warming is increased (in these simulations there was an approximate increase of 5 K), however the surface forcing, per cloud optical depth, is decreased, becoming negative for

cloud optical depths as small as  $\tau = 5$ . Similar to the dusty simulations, the increase in relative humidity (50% to 100% in these simulations) decreases the total number of clouds and the average optical depth of the clouds. However, with the additional greenhouse warming from the higher relative humidity, the loss of cloud forcing does not lead to a cooler surface like that seen in the dust simulation. This is due to the difference in absorption between dust and water vapor at solar wavelengths; dust absorbs much more readily at solar wavelengths than does water vapor leading to an effective lower atmospheric albedo and a loss of solar flux to the surface. Surface temperatures are higher for increasing levels of relative humidity. However, the overall increase in atmospheric temperature also leads to fewer and thinner clouds. So while carbon dioxide clouds warm the surface for all levels of relative humidity, the amount they do so is less for higher relative humidity than for lower relative humidity.

With water vapor in the atmosphere the formation of water clouds is likely. Water clouds complicate the problem in a number of ways. Assuming the majority of these clouds form at relative low altitude, increases in albedo at solar wavelengths and absorption in the infrared will provide a negative forcing and cool the surface. Possibly more important is the role water clouds may play in terms of nucleation. Water clouds may scavenge dust and other aerosols lifted from below making the nucleation of CO<sub>2</sub> clouds at high altitude more difficult. The presence of water clouds would therefore decrease the frequency of CO<sub>2</sub> clouds.

### 7.2.3 Carbon Dioxide Abundance

Of course both dust and water vapor would have existed in the early Martian atmosphere. The remaining simulations presented below assume a relative humidity of 50% and the baseline dust profile described above. The principle effect of increased atmospheric pressure is to saturate a larger portion of the atmosphere with respect to CO<sub>2</sub>. This in turn leads to an increase in cloud optical depth and vertical extent. For a surface pressure of 0.5 bars the region of saturation extends about 10 km centered at 20 km. For a surface pressure of 5.0 bars this saturated region extends from about 10 km above the surface to as high as 40 km.

The thicker cloud decks associated with higher pressures affect the average cloud forcing in two ways. First, for higher surface pressures, clouds are present more of the time. Secondly, the clouds that are present are thicker and thus have a higher optical depth. These two effects tend to offset each other; a higher cloud frequency leads to more warming per unit time, while thicker clouds, with their high albedo cool the surface.

Figure 18 shows the calculated temperature profiles for several different surface pressures of carbon dioxide. Below approximately 10 km the temperature profile follows a dry adiabat. Above this altitude carbon dioxide may condense, depending on the surface pressure. Where there is condensation occurring, latent heating maintains the temperature profile along the saturation temperature of CO<sub>2</sub>. The height and extent of this saturated region varies greatly with surface pressure. For all surface pressures the

base of the saturated region begins near 10 km. However, for increasing surface pressure, the top of the saturated region is extended to higher and higher altitudes.

Figure 19 shows the surface temperature as a function of time for simulations done at different surface pressures. These surface temperatures have been smoothed over 5 day moving window for clarity. The arrows on the right vertical axis of Figure 19 indicate the corresponding surface temperatures that result if the clouds radiative effects are set to zero. In each case the presence of CO<sub>2</sub> clouds warms the surface above what Kasting (1991) predicted for an atmosphere in which CO<sub>2</sub> was condensing. However, this warming is not as great as reported by either Forget and Pierrehumbert (1997) or Mischna et al. (2000). The reason for the difference is that, in our simulations, a cloud deck of appreciable optical depth does not last longer than a few days at a time. If the time average cloud optical depth, which is slightly less than one, is used to compare with these previous studies then they agree very well.

The rate of cloud formation will depend on the supply of nucleating particles into the region of supersaturation. Mixing times in this model, based on the calculated eddy mixing coefficients, ranged from several days to years. The shortest mixing times are associated with turbulent instability at the cloud level itself. This instability results from the rapid release of latent heat during cloud formation and works to mix heat and cloud particles into and out of the region. Outside of the region of cloud formation the atmosphere is more stable and has mixing times significantly less than this. Dynamic supply of dust from below may be important, however, other aerosols not considered here, such as sulfates, may be more common at these altitudes.

The amount of warming that a scattering CO<sub>2</sub> cloud provides depends on the total abundance of carbon dioxide. Figure 20 shows the difference in average surface temperature with and without cloud scattering included as a function of CO<sub>2</sub> surface pressure. The maximum cloud warming occurs for CO<sub>2</sub> surface pressures of approximately 1 bars. For CO<sub>2</sub> surface pressures less than 1 bars the change in planetary albedo resulting from cloud formation is more significant than at high pressures. Furthermore, at lower pressures, clouds are not present as frequently as at higher pressures. Hence the clouds do not yield significant forcing at lower pressures. The decrease in the ability of clouds to warm the surface at CO<sub>2</sub> pressures greater than about 1 bars is the combined result of two factors. First, the frequency of clouds that have opacities greater than  $\tau = 10$ , which cool rather than warm the surface, becomes significant ( $> 10\%$ ) for surface pressures greater than about 1 bars. Secondly, the feedback between atmospheric water vapor and the surface temperature can contribute to the reduced effectiveness of CO<sub>2</sub> clouds. As the surface temperature warms more water vapor is allowed into the atmosphere. At surface pressures below 1 bars the additional greenhouse warming contributes significantly to the surface temperature. However, as the surface temperature further increases with increasing CO<sub>2</sub> pressure, there comes a point when so much water vapor enters the atmosphere, that the atmosphere between the cloud and the surface becomes "opaque" at infrared wavelengths. Thus, for surface pressures greater than about 1 bars, the contribution from the cloud decreases systematically.

## 8.0 Conclusions

The measurements by Glandorf et al. (this issue) allow numerical treatment of carbon dioxide cloud formation and a much better understanding of cloud properties under various climate conditions. The formation of carbon dioxide clouds proceeds in a similar fashion as that of terrestrial cirrus clouds; both require supersaturations of about 35% for ice crystals to form and exhibit rapid condensation once nucleation has occurred. The difference in resulting cloud properties, such as larger particle size on Mars, is simply the result of the much greater mass of carbon dioxide available to condense on Mars, as compared to water vapor on Earth. To achieve the critical nucleation supersaturation, temperature declines of several degrees below the CO<sub>2</sub> vapor saturation temperature are required. Therefore, under most circumstances the initiator of carbon dioxide clouds will be dynamically driven cooling events such as atmospheric wave activity, rather than diabatic cooling.

The cold temperatures measured by Mars Pathfinder near 80 km are believed to be the result of vertically propagating thermal tides (Haberle et al. 1999; Magalhaes et al. 1999). If there is a sufficient source of dust in these high altitudes CO<sub>2</sub>, clouds can form in this region. Because of the strong dependence on available nucleating site (assumed here to be dust) the appearance of these high altitudes hazes may be indicators of strong vertical mixing associated with dust storms. Even relatively small regional dust storms can enhance the strength of the Hadley circulation causing it to rise to altitudes as high as 70 km. Dust carried upward in these periods of strong circulation would allow for the formation of high altitude tropical CO<sub>2</sub> clouds. However, these CO<sub>2</sub> clouds contain relatively large particles, not the small ones suggested by Clancy and Sandor (1998) to cause the Pathfinder blue clouds.

With the model developed here, we have been able to answer some of the key questions regarding the formation of carbon dioxide clouds in the early Martian atmosphere. Carbon dioxide clouds generally contain large particles with average radii greater than 1000  $\mu\text{m}$  (although convective clouds may contain smaller particles). Whether or not these clouds provide net warming to the surface depends strongly on the amount of other infrared absorbers in the atmosphere, including dust and water vapor. In a dust free atmosphere, a cloud with an optical depth of  $\tau = 10$  ( $\tau = 10 \mu\text{m}$ ) will have a strong positive forcing at the surface. For an atmosphere containing radiatively active dust, due to an increase in absorption of scattered infrared flux, the radiative forcing for a similar cloud can be reduced to nearly half that of the dust free case. Likewise, water vapor can reduce the ability of a cloud to warm the surface. For an atmosphere in which the troposphere is saturated with water, the cloud forcing is moderated, leading to less surface warming associated with the cloud. In both cases, the presence of atmospheric water vapor or dust warms the atmosphere, thereby reducing the total amount of carbon dioxide cloud formation.

When clouds are allowed to form freely in the model the resulting radiative forcing leads to warming of the atmosphere, which in turn dissipates the clouds. This warming

combined with release of latent heat and cloud particle sedimentation, never allows an optically thick cloud to exist for any longer than about 10 days. The time average optical depth is approximately  $\tau = 1$  (at  $\lambda = 10 \mu\text{m}$ ). Therefore, there is some warming of the surface as a result of clouds, albeit limited to a much smaller amount than proposed by Forget and Pierrehumbert (1997) and Mischner et al. (2000). We conclude that carbon dioxide atmospheres with surface pressures of 5 bars or less are unlikely to have lifted the mean temperature of Mars above the freezing point when the solar luminosity was 75% of current values.

### Acknowledgements

This work was sponsored by NASA's Astrobiology Program, NCC2-5300 and NCC2-1052 and NASA's Planetary Atmospheres Program NAG5-6900.

### References

- Carr, M. H. 1986. Mars: A water rich planet? *Icarus* **56**, 187-216.
- Christensen, P. R., D. L. Anderson, S. C. Chase, R. T. Clancy, R. N. Clark, B. J. Conrath, H. H. Kieffer, R. O. Kuzmin, M. C. Malin, J. C. Pearl, T. L. Roush and M. D. Smith 1998. Results from the Mars Global Surveyor Thermal Emission Spectrometer, *Science* **279**, 5357.
- Clancy, R. T., and B. J. Sandor 1998. CO<sub>2</sub> ice clouds in the upper atmosphere of Mars *Geophys. Res. Lett.*, **25**, 489-492.
- Clark, R. N., F. P. Fanale, and A. P. Zent, 1983. Frost grain size metamorphism: Implications for remote sensing of planetary surfaces, *Icarus* **56**, 233-245.
- Colaprete, A., O. B. Toon, and J. A. Magalhães 1999. Cloud formation under Mars Pathfinder conditions, *J. Geophys. Res.* **104**, 9043-9054.
- Forget, F. and R. T. Pierrehumbert. 1997. Warming early Mars with carbon dioxide clouds that scatter infrared radiation. *Science* **278**, 1273-1276.
- Forget, F., and J. B. Pollack, 1996. Thermal infrared observations of the condensing Martian polar caps: CO<sub>2</sub> ice temperatures and radiative budget, *J. Geophys. Res.* **101**, 16,865-16,879.
- Forget, F., F. Hourdin, and O. Talagrand, 1997. CO<sub>2</sub> snowfall on Mars: simulated with a general circulation model, *Icarus* **131**, 302-316.

- Gough, D. O. 1981. Solar interior structures and luminosity variations. *Solar Phys.* **74**, 21-34.
- Haberle, R. M., H. C. Houben, R. Hertenstein, and T. Herdtle, 1993. A boundary-layer model for Mars: Comparison with Viking Lander and entry data, *J. Atmos. Sci.* **50**, 1544-1559.
- Haberle, R. M., M. M. Joshi, J. R. Murphy, J. R. Barnes, J. T. Schofield, G. Wilson, M. Lopez-Valverde, J. L. Hollingsworth, A. F. C. Bridger, and J. Schaeffer 1999. GCM simulations of the Mars Pathfinder ASI/MET data, *J. Geophys. Res.* **104**, 8957-8974.
- Hansen, B. H., 1999. Control of the radiative behavior of the Martian polar caps by surface CO<sub>2</sub> ice: Evidence from Mars Global Surveyor measurements, *J. Geophys. Res.* **104**, 16,471-16,486.
- Hansen, G. B., 1997a. The infrared absorption spectrum of carbon dioxide ice from 1.8 to 333  $\mu\text{m}$ . *J. Geophys. Res.* **102**, 21,569-21,587.
- Hansen, G. B., 1997b. Spectral absorption of solid CO<sub>2</sub> from the ultraviolet to the far-infrared, *Adv. Space Res.* **20**, 1613-1616.
- Herr, K. C., and G. C. Pimentel 1970. Evidence for solid carbon dioxide in the upper atmosphere of Mars, *Science*, **167**, 47-49.
- Hinson, D. P., F. M. Flasar, R. A. Simpson, J. D. Twicken and G. L. Tyler 1999. Initial results from radio occultation measurements with Mars Global Surveyor, *J. Geophys. Res.* **104**, 26997-27012.
- Hunt, G. E., 1980. On the infrared radiative properties of CO<sub>2</sub> ice clouds: Application to Mars, *Geophys. Res. Lett.* **7**, 481-484.
- Jaquin, F., P. Gierasch, and R. Kahn 1986. The vertical structure of limb hazes in the Martian atmosphere, *Icarus* **68**, 442-461.
- Jensen, E. J., O. B. Toon, A. Tabazadeh, G. W. Sachse, B. E. Anderson, K. R. Chan, C. W. Twohy, B. Gandrud, S. M. Aulenbach, A. Heymsfield, J. Hallett, and B. Gary 1998. Ice nucleation processes in upper tropospheric wave-clouds observed during SUCCESS, *Geophys. Res. Lett.* **25**, 1363-1366.
- Kasting, J. F., 1991. CO<sub>2</sub> condensation and the climate of early Mars. 1991. *Icarus* **94**, 1-13.
- Kasting, J. F., J. B. Pollack, and D. Crisp 1984b. Effects of high CO<sub>2</sub> levels on surface temperature and atmospheric oxidation state of the early Earth. *J. Atmos. Chem.* **1**, 403-428.

- Kieffer, H. H., S. C. Chase, E. D. Miner, F. D. Palluconi, G. Münch, G. Neugebauer, and T. Z. Martin 1976. Infrared thermal mapping of the Martian surface and atmosphere: First results, *Science* **193**, 780-786.
- Kieffer, H., T. Titus, K. Mullins, 1998. Early TES Observations of the South Polar Region, In Lunar and Planetary Science XXIX, Abstract 1481, Lunar and Planetary Institute, Houston (CD-ROM)
- Magalhaes, L. A., J. T. Schofield, A. Seiff 1999 Results of the Mars Pathfinder atmospheric structure investigation. *J. Geophys. Res.* **104**, 8943-8956.
- Michelangeli, D. V., O. B. Toon, R. M. Haberle, and J. B. Pollack 1993. Numerical simulation of the formation and evolution of water ice clouds in the Martian atmosphere, *Icarus* **100**, 261-285.
- Mischna, M. A., J. F. Kasting, A. Pavlov, and R. Freedman 2000. Influence of carbon dioxide clouds on early Martian climates. *Icarus* **145**, 546-554.
- Murphy, J., J. B. Pollack, R. M. Haberle, C. B. Leovy, O. B. Toon, and J. Schaeffer 1995. Three dimensional numerical simulation of Martian global dust storms. *J. Geophys. Res.* **100**, 26,357-26,376.
- Paige, D. A., and A. P. Ingersoll 1985. Annual heat balance of Martian polar caps: Viking observations. *Science* **228**, 1160-1168.
- Pettengill, G. H., P. G. Ford, 1999. Winter clouds over the north Martian polar cap.
- Pierrehumbert, R. T. and C. Erlick. 1997. On the scattering greenhouse effect of CO<sub>2</sub> ice clouds. *J. Atmos. Sci.* **55**, 1897-1903.
- Pollack, J. B. 1979. Climate change on the terrestrial planets. *Icarus* **37**, 479-553.
- Pollack, J. B., J. F. Kasting, S. M. Richardson, and K. Poliakoff 1987. The case for a wet, warm climate on early Mars. *Icarus* **71**, 203-224.
- Sagan, C., and G. Mullen 1972. Earth and Mars: Evolution of atmospheres and surface temperatures. *Science* **177**, 52-56.
- Tabazadeh, A., O. B. Toon, and E. Jensen 1997. Formation and implications of ice particle nucleation in the stratosphere. *Geophys. Res. Lett.*, **24**, 2007-2010.
- Toon, O. B., R. P. Turco, J. Jordan, J. Goodman, and G. Ferry 1989. Physical processes in polar stratospheric ice clouds, *J. Geophys. Res.* **94**, 11,359-11,380.
- Wood, S. E., 1999. Nucleation and growth of CO<sub>2</sub> ice crystals in the Martian atmosphere, *UCLA Dissertation*, PN AAT 9926317.

Young, J. B., 1993. The condensation and evaporation of liquid droplets at arbitrary Knudsen number in the presence of an inert gas, *Int. J. Heat Mass Transfer.* **36**, 2941-2956.

Figure 1. The calculated heterogeneous nucleation rate of CO<sub>2</sub> on ice as a function of supersaturation, contact parameter and nucleating particle radius.

Figure 2. (a) The simulated effective radius (physical cross section weighted average) of CO<sub>2</sub> ice particles vs. the ambient air-cooling rate for three different contact parameters at Martian surface pressures. For larger contact parameters more particles are nucleated, leading to reduced particle size. (b) The simulated maximum number of CO<sub>2</sub> ice particles vs. the ambient air-cooling rate for three different contact parameters. The larger the contact parameter the more small particles are able to nucleate. 100 cm<sup>-3</sup> is the maximum possible number of particles that could form in these simulations.

Figure 3. The temperature at which the nucleation rate is equal to  $J = 1 \text{ sec}^{-1}$  is shown for three nucleating dust particle radii:  $r = 0.005$  (dotted line),  $0.01$  (dash-dot-dot),  $0.1 \text{ } \mu\text{m}$  (solid). A contact parameter of  $m = 0.95$  was assumed. Also plotted are the (Pathfinder) Mars Pathfinder entry profile, (RO) MGS radio occultation measurement, (GCM) a polar temperature profile from the Ames Mars GCM near winter solstice and (radiative equilibrium) the radiative equilibrium temperatures at winter solstice. The curve labeled with  $s = 1$  is the vapor pressure curve at which the saturation ratio is equal to one. To the right of this curve particles will evaporate, to the left particles will condense vapor and grow.

Figure 4. The condensation growth rate for two particle radii as a function of Knudsen number. The (right-hand) vertical axis gives the pressure that corresponds to the Knudsen number for each of the two particles. The two growth curves are for the condensation model presented here (Toon et al, 1989) and for the condensation model described by Young (1993). Indicated on the figure is where the approximate transition from the kinetic to diffusion regimes occurs and at what Knudsen number both current and possible past climates of Mars exist.

Figure 5. The growth rate of CO<sub>2</sub> ice as a function of supersaturation derived from absorption measurements by Glandorf et al. (this issue) (squares). The two curves shown are the growth rates predicted by the models of Toon et al. (1989) and that of Young (1993).

Figure 6. The condensation growth and fall times as a function of radius and Knudsen number. The data is for an ambient pressure of 6.2 mbar, a 5% inert gas concentration and 20% supersaturation. Indicated on the plot by the dotted line is the approximate location where the transition from kinetic to diffusion regimes occurs.

Figure 7. The cloud particle effective radius and mass mixing ratio as functions of time. The cloud was formed by a 3 hour cooling wave of  $6.5 \text{ K hour}^{-1}$  centered at 82 km. The dashed line in the right panel indicates a mass mixing ratio of 35%, corresponding to the required supersaturation for nucleation.

Figure 8. The cloud particle effective radius and mass mixing ratio as functions of time. The cloud was formed by a 3 hour cooling with a rate of  $6.5 \text{ K hour}^{-1}$  centered at 60 km.

The dashed line in the right panel indicates a mass mixing ratio of 35%, corresponding to the required supersaturation for nucleation.

Figure 9. Temperature profiles calculated by three radiative-convective (RC) models. The model by Pollack et al. (1987) is a standard RC model and does not treat carbon dioxide condensation. The models by Kasting (1991) and Forget and Pierrehumbert (1997) examined the effects of a CO<sub>2</sub> cloud on the RC solution and found that they could either warm or cool the planet depending on cloud characteristics. Calculations were done for 2 bars of CO<sub>2</sub> and a solar luminosity 75% that of the current value.

Figure 10. The fractional percent difference between the transmissions calculated from Eq. 6.2.2 and Eq. 6.2.6 for several values of the binary species coefficient ( $\eta$ ) at  $\nu = 3580$  cm<sup>-1</sup>. A binary species coefficient of 0.9 is equivalent to a water mixing ratio of 6.6%. Calculations are for an atmosphere containing 0.5 bars of CO<sub>2</sub>.

Figure 11. (a) The top-of-the-atmosphere radiative forcing as a function of cloud optical depth is calculated for a stationary cloud at 17 km composed of particles with a single radius for several cloud particle sizes. (b) The surface radiative forcing as a function of cloud optical depth is calculated for a stationary cloud at 17 km composed of particles with a single radius for several cloud particle sizes.

Figure 12. (a) The up, down and net solar (top panel) and infrared (bottom panel) radiative fluxes for a cloud free atmosphere containing 2 bars of CO<sub>2</sub>. (b) The up, down and net solar (top panel) and infrared (bottom panel) radiative fluxes for an atmosphere containing 2 bars of CO<sub>2</sub> with a CO<sub>2</sub> cloud centered at 25.5 km. The cloud was approximately 5 km thick with a total optical depth of  $\tau = 10$ .

Figure 13. The temperature profiles for a 2 bars atmosphere with (solid line) and without clouds (dotted line). For both simulations no dust radiative effects were included. The saturation of CO<sub>2</sub> is indicated by the dot-dashed line.

Figure 14. Top-of-the-atmosphere and surface radiative forcing as a function of cloud optical depth for a stationary cloud at 17 km composed of 10  $\mu$ m CO<sub>2</sub> ice particles with atmospheric dust is included. The optical depth of the dust at the surface is  $\tau = 0.25$  at  $\lambda = 0.65$   $\mu$ m.

Figure 15. The integrated surface cloud optical depth averaged over a 5 day moving window for simulations with (solid line) and without (dashed line) dust radiative effects. Calculations were done for 2 bars of CO<sub>2</sub> and a solar luminosity 75% that of the current value.

Figure 16. The surface temperatures as a function of time for simulations with and without dust radiative effects included. Calculations were done for 2 bars of CO<sub>2</sub> and a solar luminosity 75% that of the current value.

Figure 17. The surface temperature as a function of time for two abundances of water vapor, 50% and 100 % at all levels, in a 2 bar CO<sub>2</sub> atmosphere. For these simulations the radiative effects of dust were set to zero.

Figure 18. Temperature profiles for several surface pressures of carbon dioxide. Each profile was taken on day number 150 of each simulation (solar luminosity equal to 75% present luminosity).

Figure 19. The surface temperature for several surface pressures as a function of time. Both dust and water vapor radiative effects were included (solar luminosity equal to 75% present luminosity). The arrows along the right vertical axis indicate the surface equilibrium surface temperature for the same pressures but with the radiative effects of the clouds set to zero.

Figure 20. The difference in average surface temperature for simulations with and without clouds. Calculations were done for 2 bars of CO<sub>2</sub> and a solar luminosity 75% that of the current value.

Figure 1

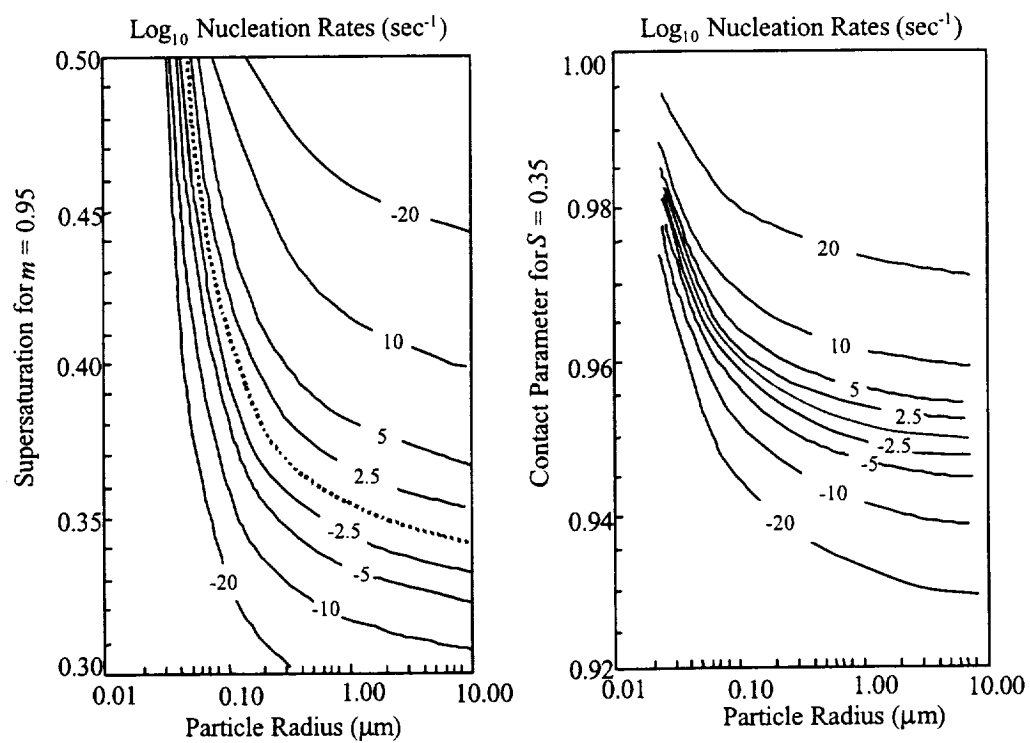


Figure 2

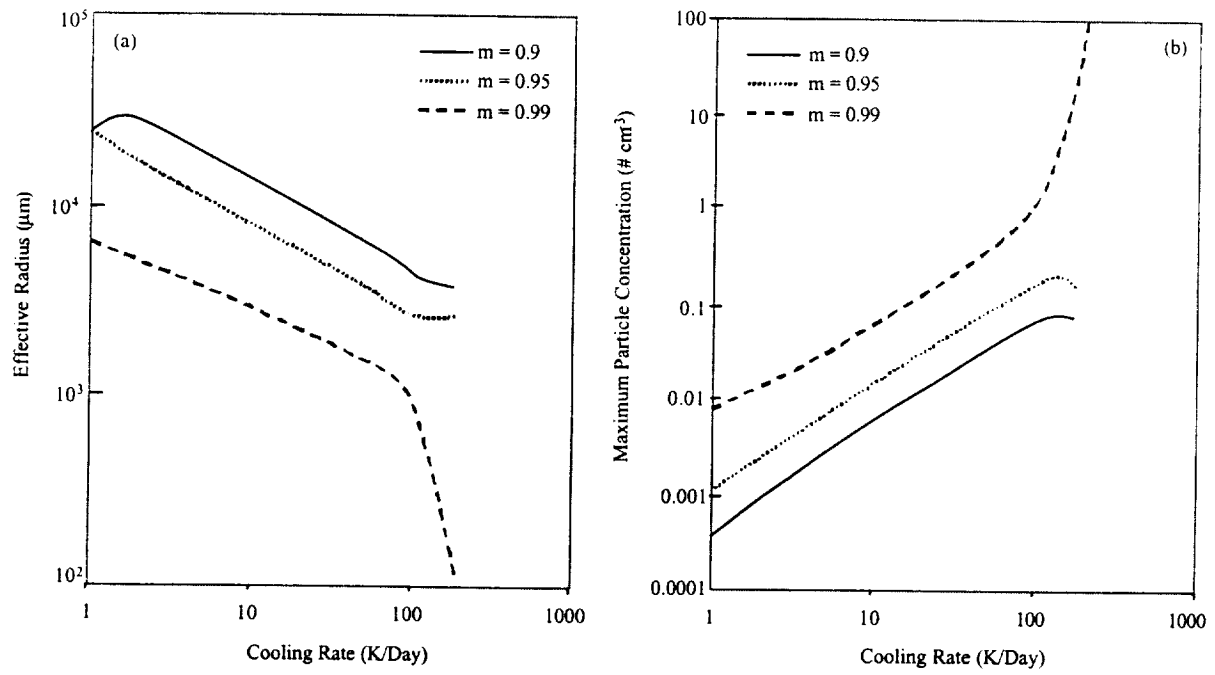


Figure 3

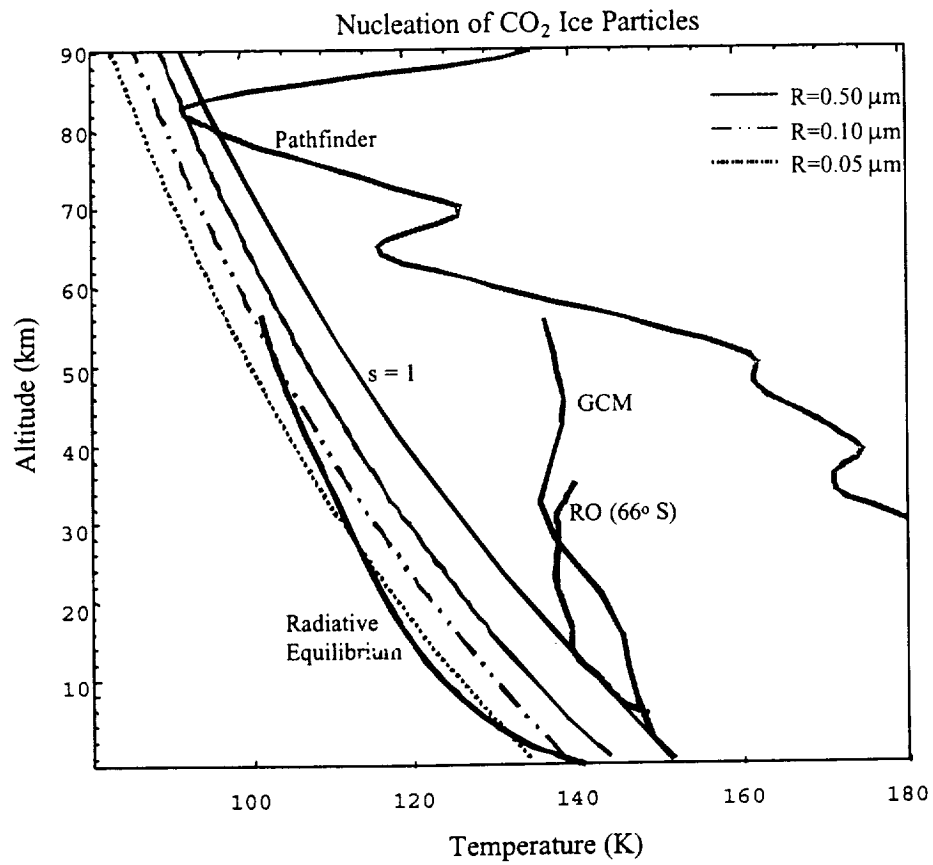


Figure 4

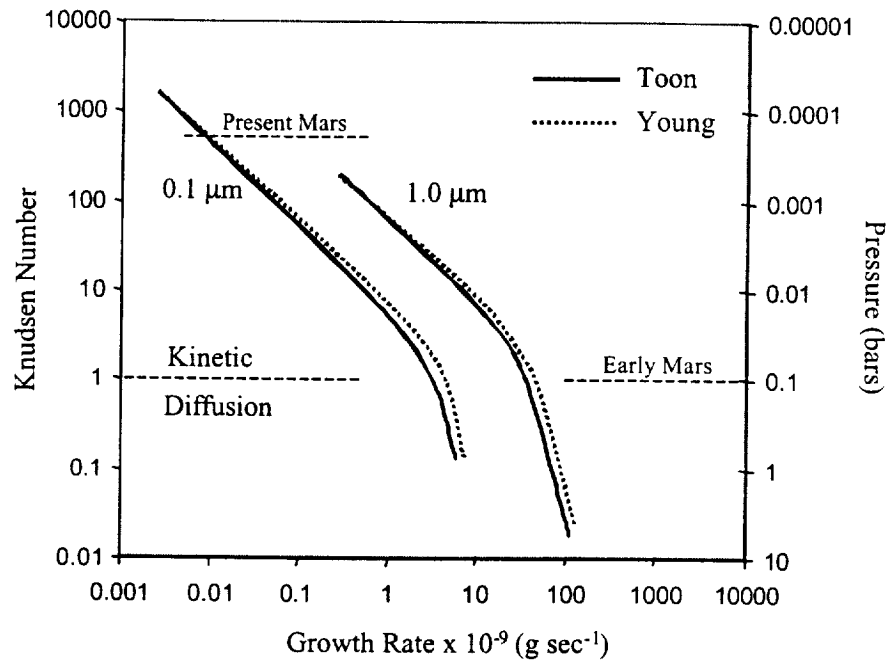


Figure 5

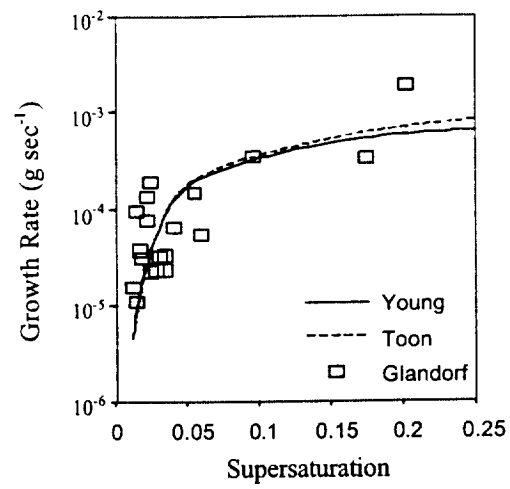


Figure 6

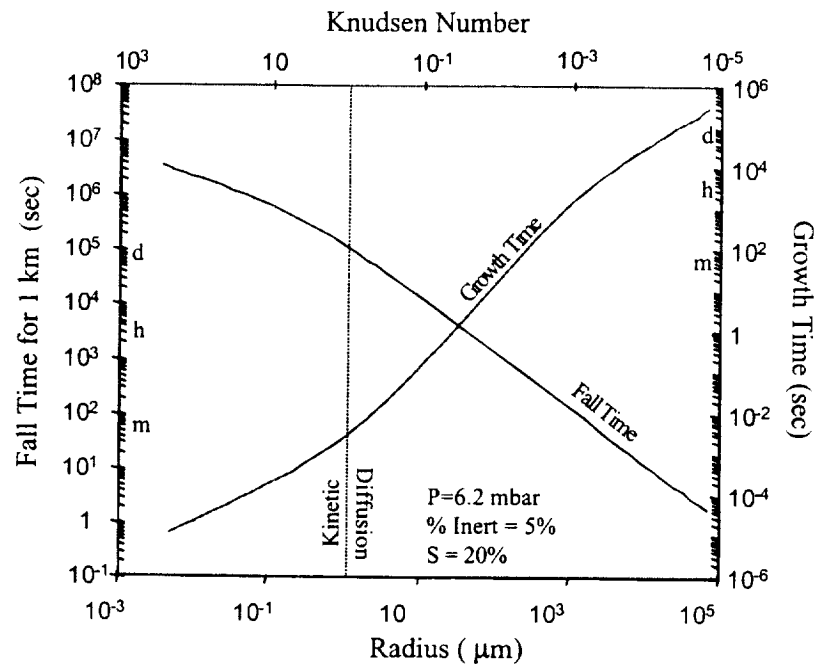
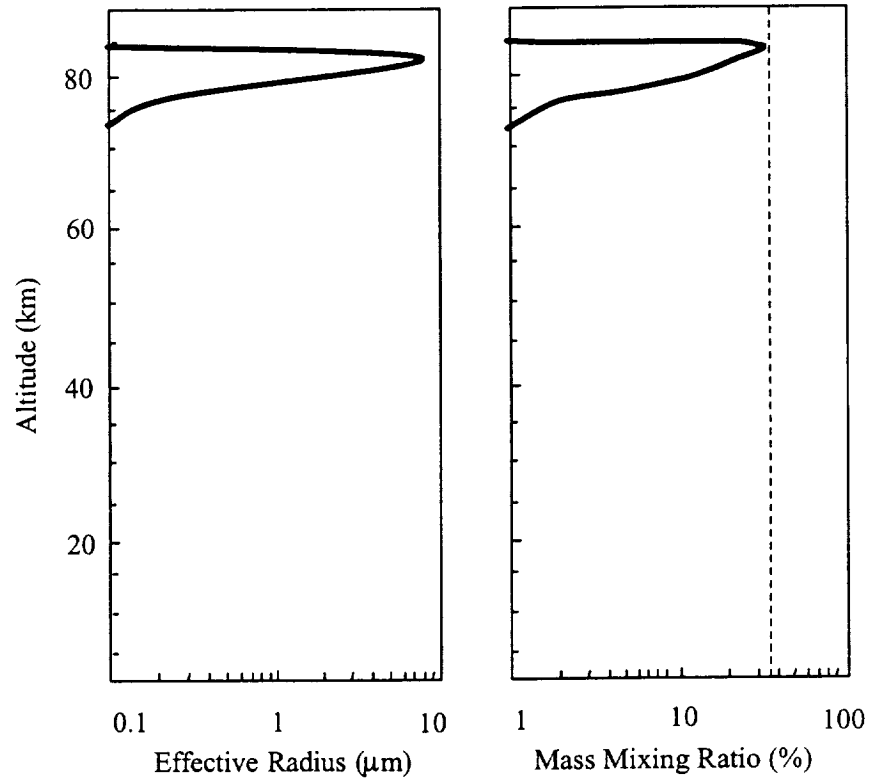


Figure 7



**Figure 8**

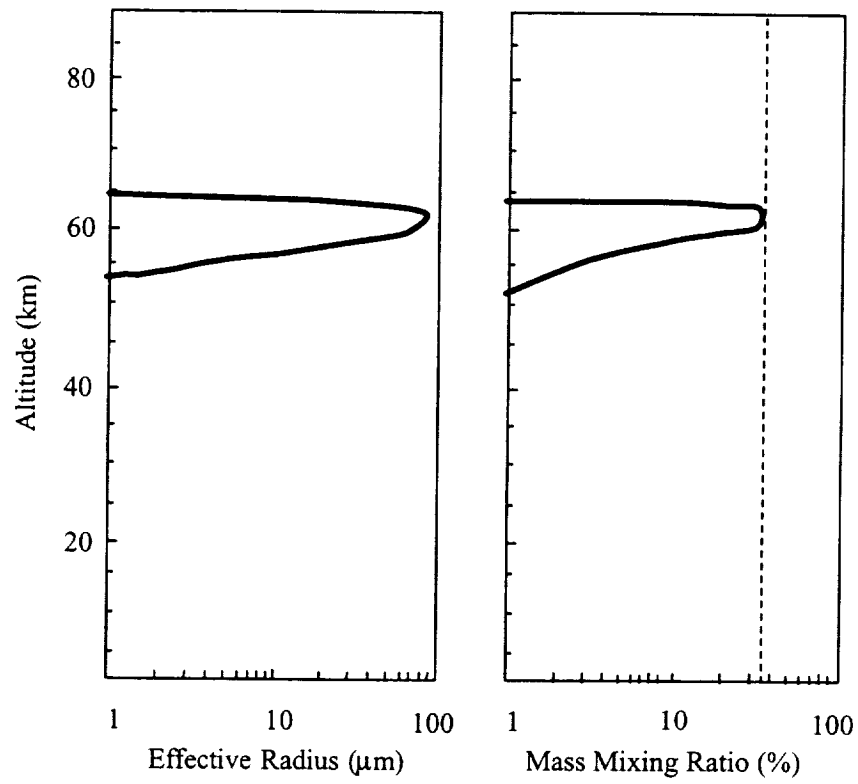


Figure 9

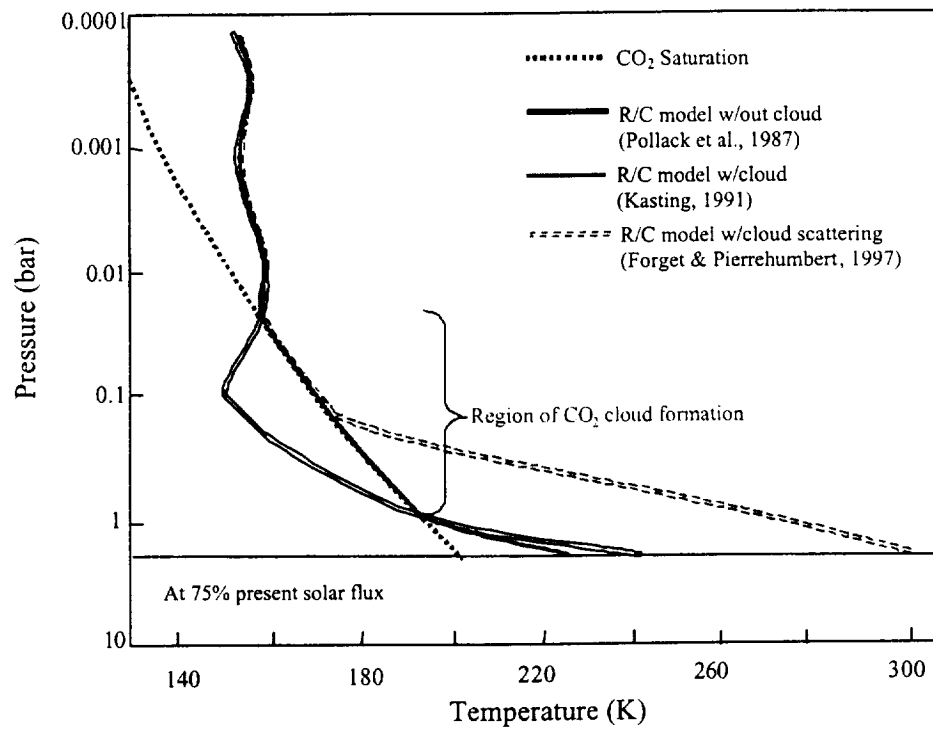


Figure 10

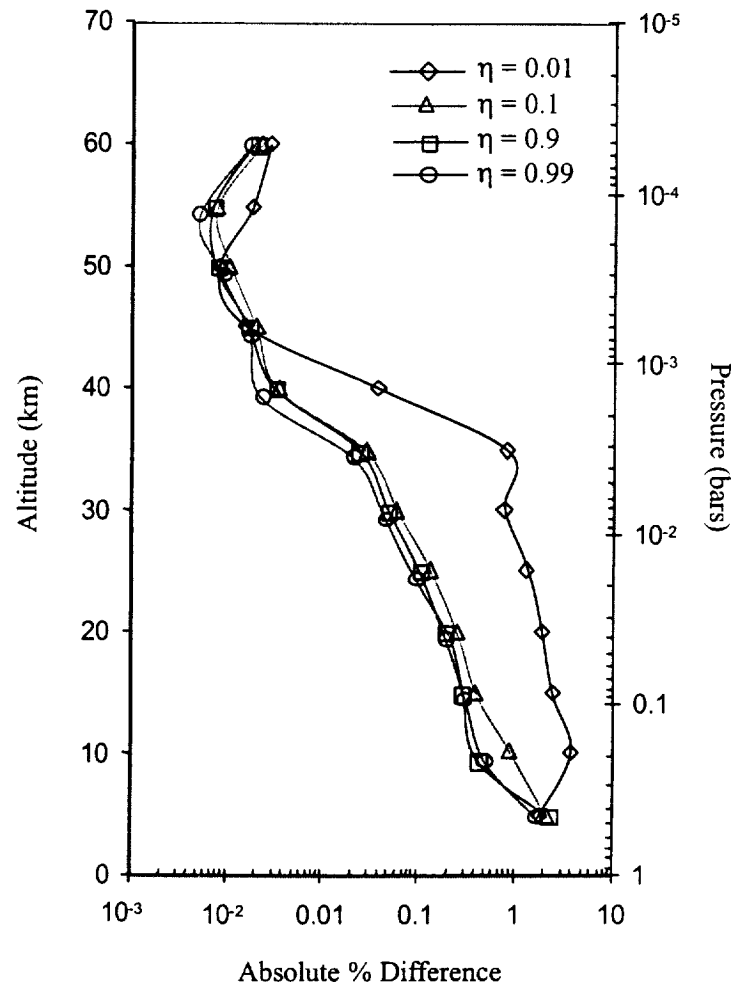


Figure 11

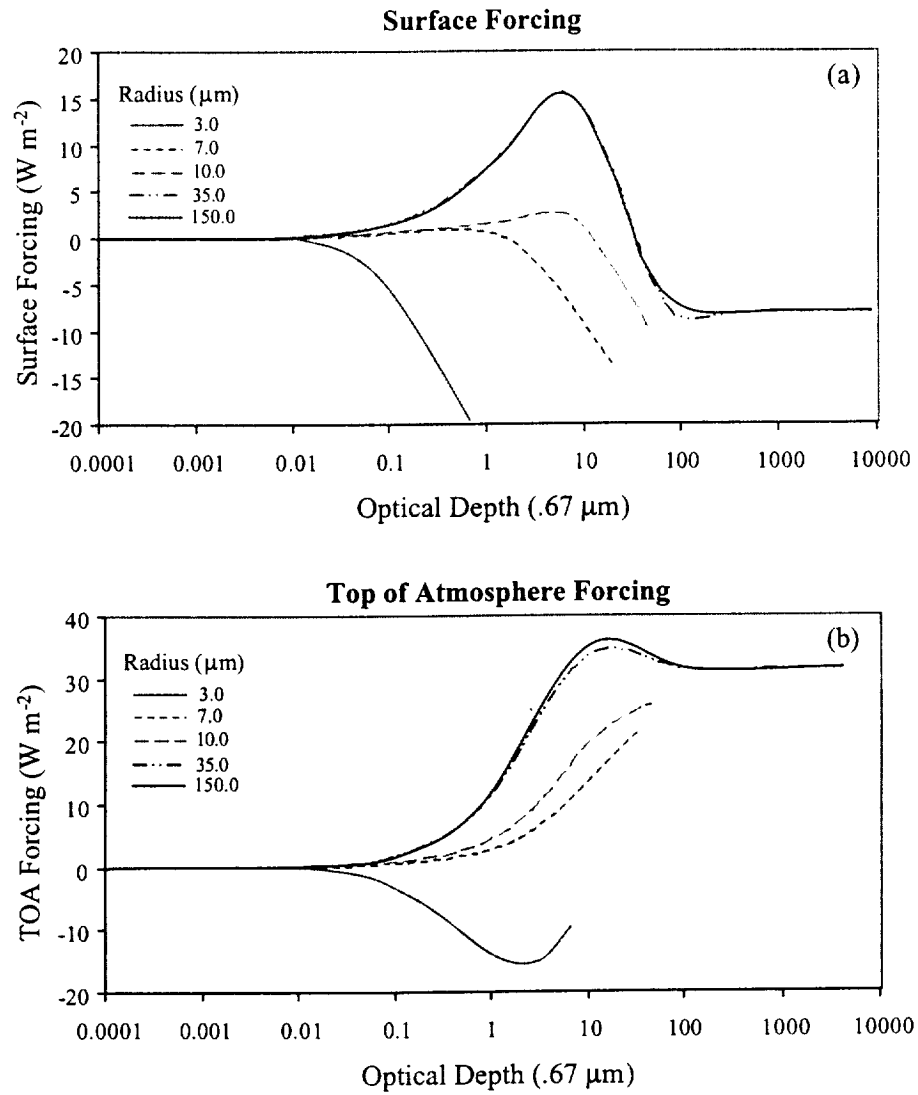


Figure 12

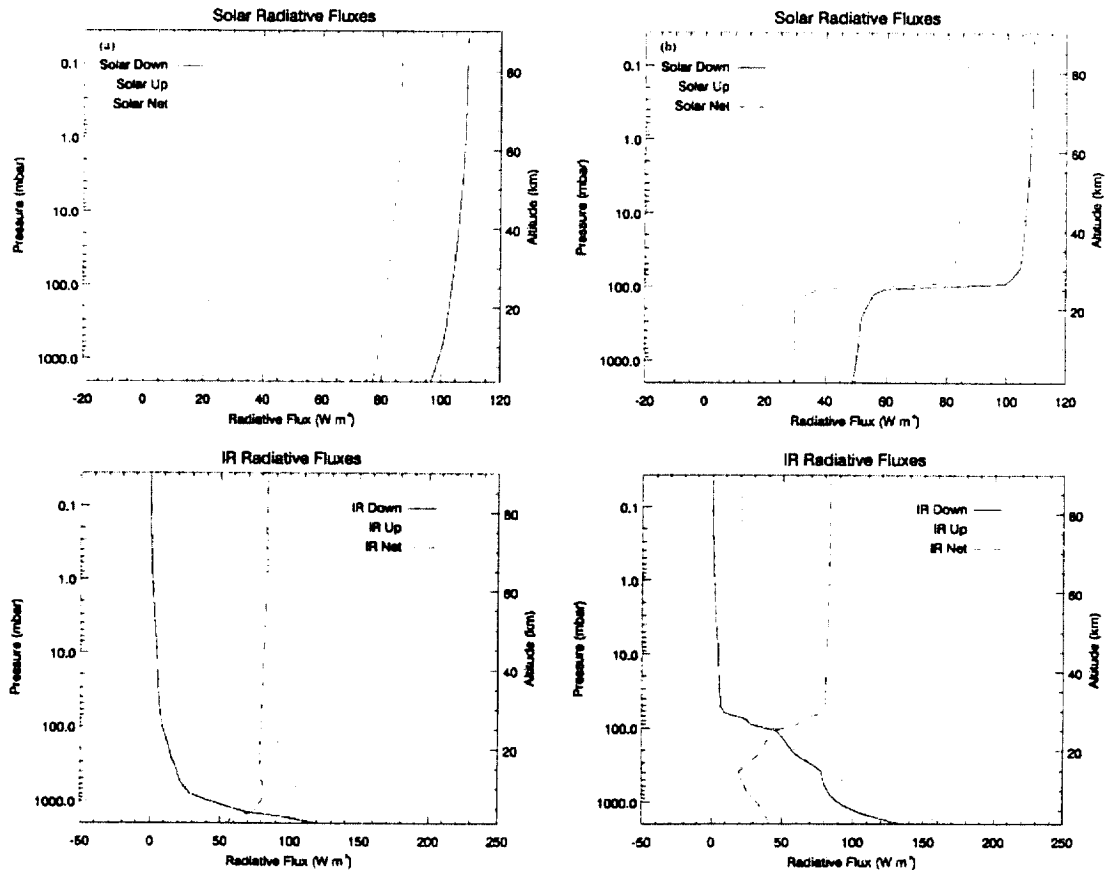


Figure 13

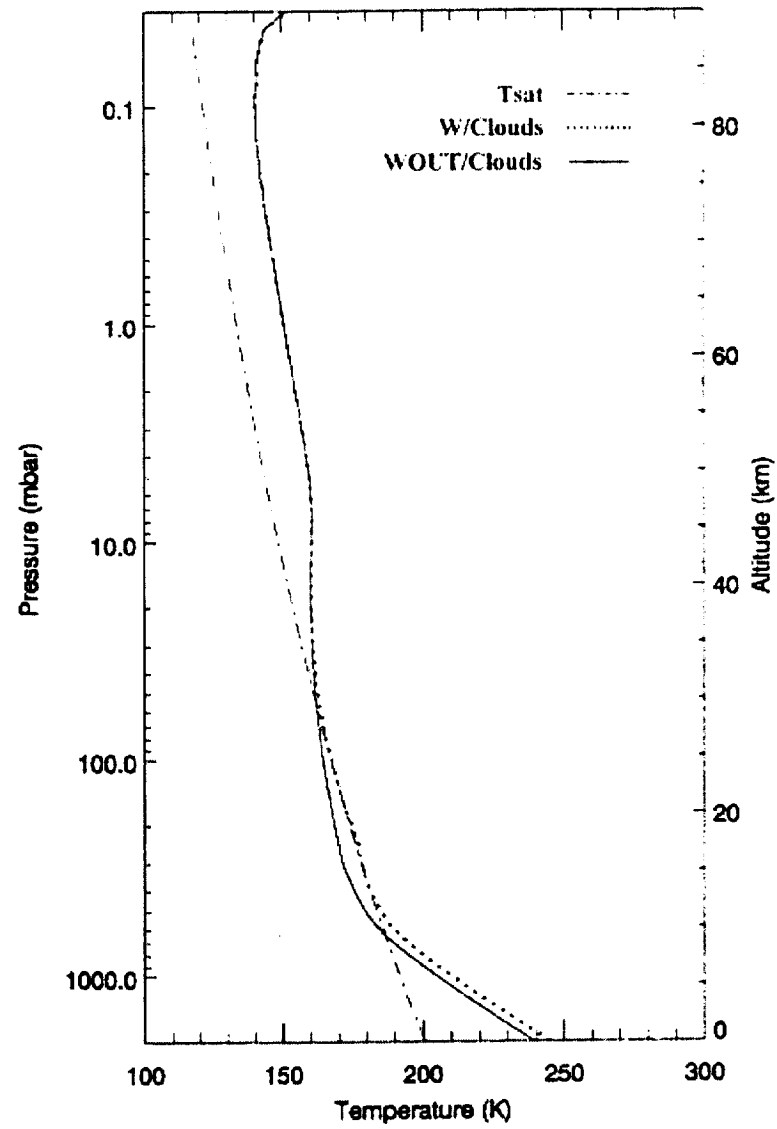


Figure14

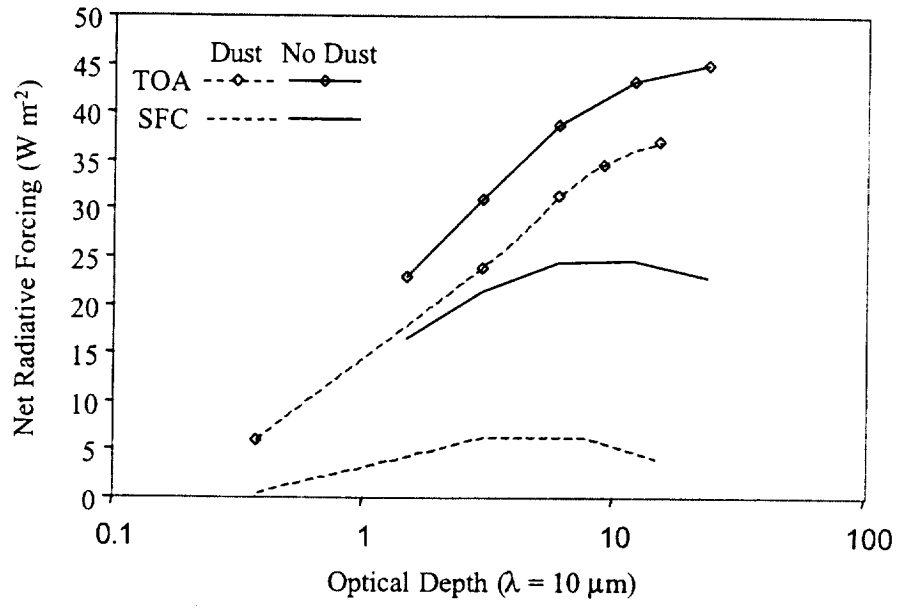


Figure 15

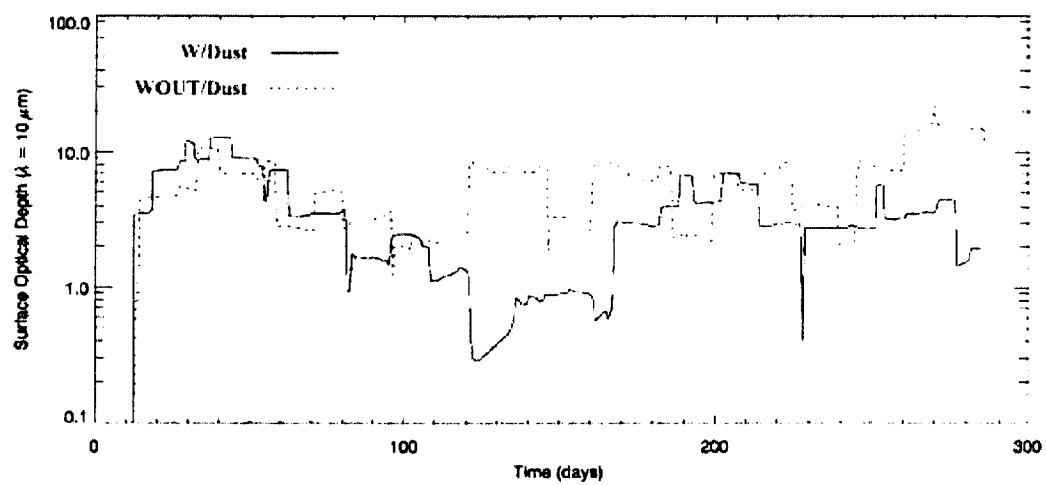


Figure 16

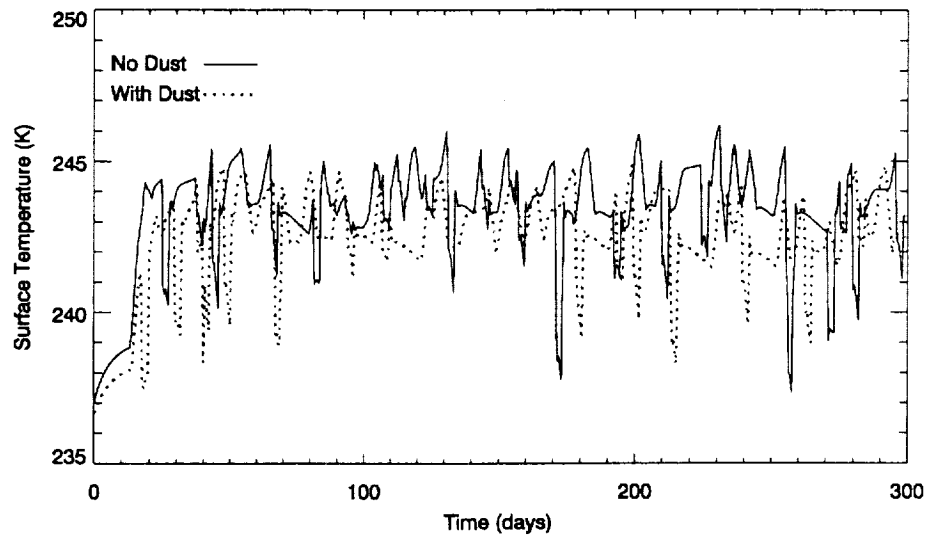


Figure 17

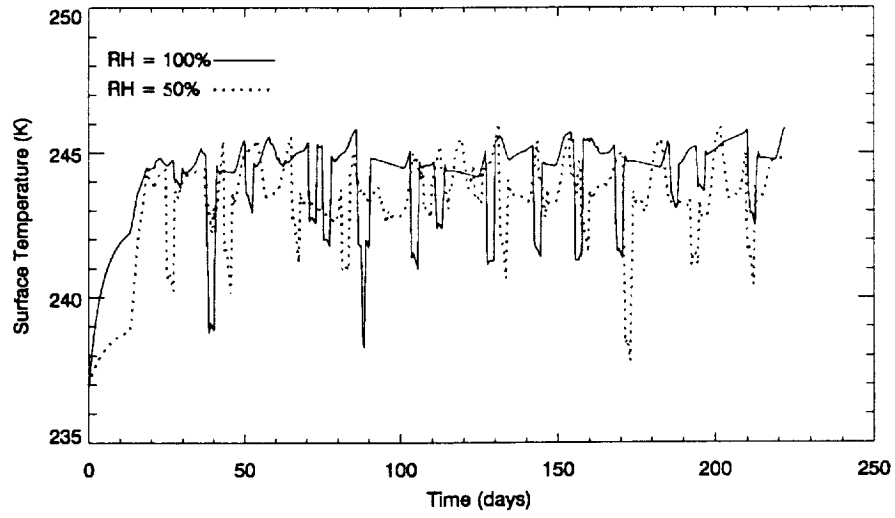


Figure 18

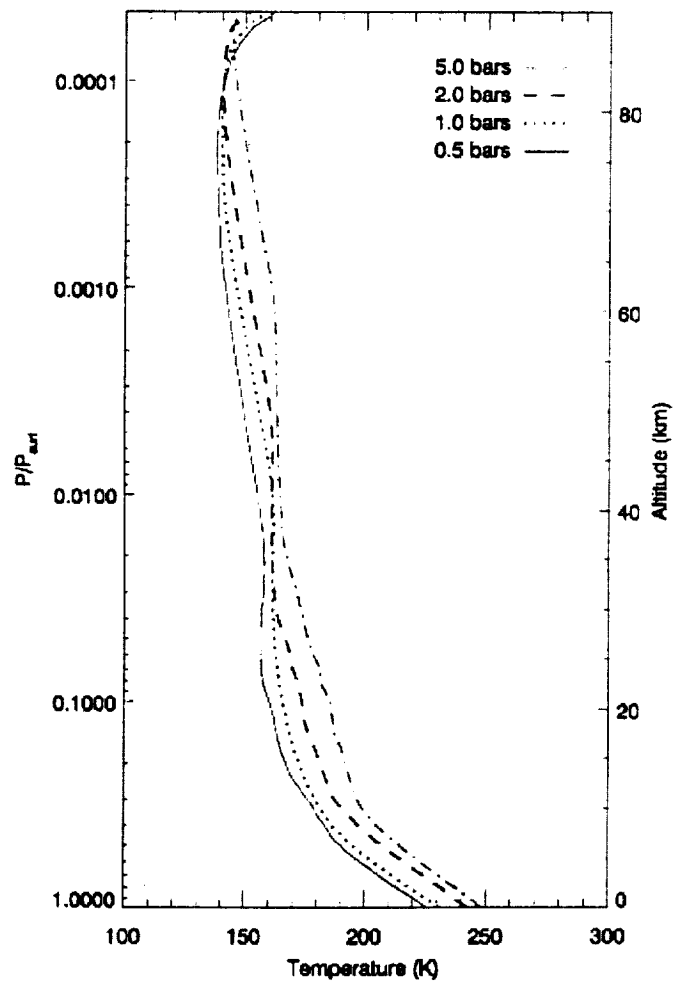
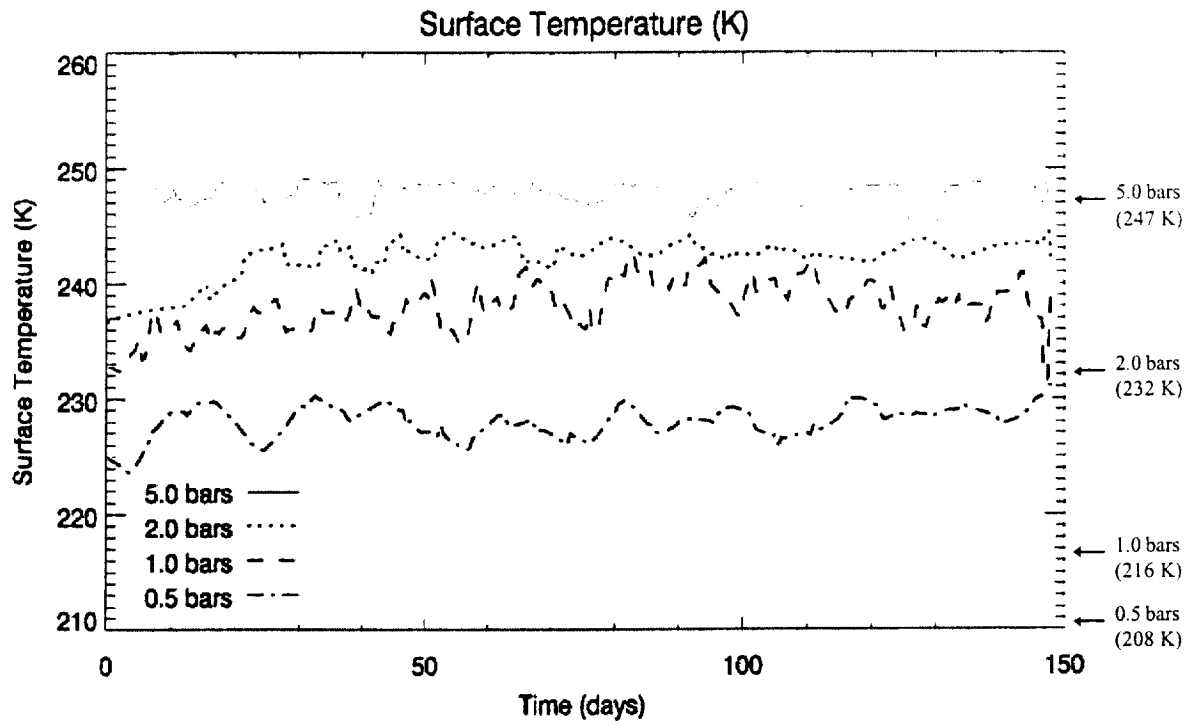
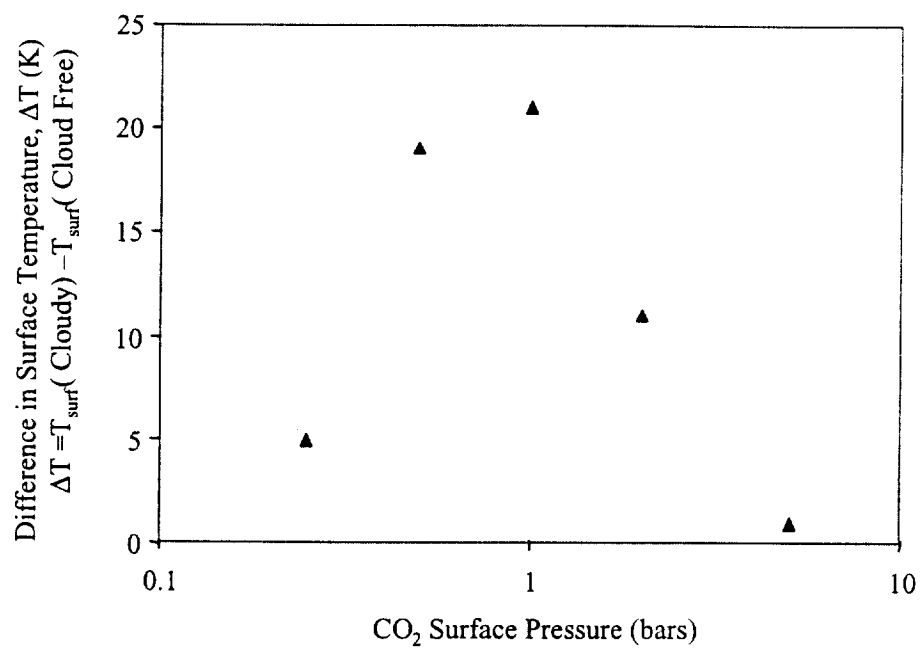


Figure 19



**Figure 20**



**Table 6.1 Spectral Bands and Key Species**

Band Number	Wavenumber Range (cm <sup>-1</sup> )	Key Species	Integrated Strengths, $S_{\dagger}$	Line
1-8	40-440	H <sub>2</sub> O, Dust	32.98	
9	440-495	H <sub>2</sub> O, Dust	1.20	
10	495-545	Dust		
11	545-617	CO <sub>2</sub> , Dust	14.4	
13	667-720	CO <sub>2</sub> , Dust	826.0	
14	720-800	CO <sub>2</sub> , Dust	18.5	
15	800-875	Dust		
16-25	875-1750	CO <sub>2</sub> , Dust	5.1	
26-29	1750-2050	CO <sub>2</sub> , Dust	22.0	
30-31	2050-2200	Dust		
32-33	2200-2397	CO <sub>2</sub>	1046.5	
33-35	2397-3087	CO <sub>2</sub> , H <sub>2</sub> O	0.3, 1.5	
36-38	3087-3760	CO <sub>2</sub> , H <sub>2</sub> O	55.0, 92.43	
39-42	3760-4950	H <sub>2</sub> O	0.02	
43-55	4950-15000	CO <sub>2</sub> , H <sub>2</sub> O	3.5, 750.0	
56-60	15000-35000	Dust		

†  $S$  is in units of  $10^{-21}$  cm (Goody and Yung, 1989)

**Table 7.1 Simulation Parameter Space**

Parameter	Value(s)
Nucleation Contact Parameter ( $m$ )	0.95
Critical Supersaturation ( $s$ )	0.35
Surface Albedo ( $\lambda = .65 \mu\text{m}$ )	0.22
Soil Thermal Inertia ( $\text{W m}^{-2} \text{sec}^{1/2} \text{K}^{-1}$ )	145.0
Dust Optical Depth ( $\lambda = 0.65 \mu\text{m}$ )	0 / 0.25
Water Relative Humidity (%)	50 / 100
CO <sub>2</sub> Abundance (bars)	0.5 / 1 / 2 / 5

